MULTISCALE MODELING OF MICROCRYSTALLINE MATERIALS

Thesis by

Daniel E. Hurtado

In Partial Fulfillment of the Requirements

for the Degree of

Doctor of Philosophy

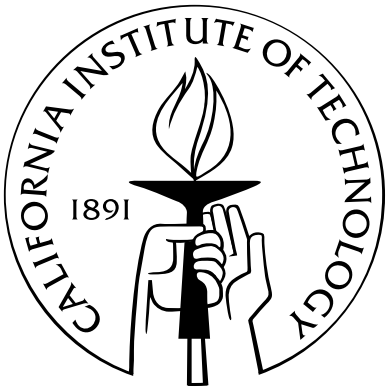

California Institute of Technology

Pasadena, California

2011

(Defended October 27, 2010)

To Margarita and Amanda.

Acknowledgements

I would like to express my deepest appreciation to Professor Michael Ortiz for his supervision, guidance and support during all these years at Caltech. His insights and constant encouragement to pursue challenging and creative ideas has made my doctoral work a very stimulating and fruitful experience. There is no doubt my passion for mechanics has been strongly influenced by him over the last four years.

I would also like to thank Professor Guruswami Ravichandran, Profesor Kaushik Bhattacharya and Professor Julia Greer for serving on my thesis committee and for their invaluable comments and suggestions on my thesis work. In particular, Professor Ravichandran has been a excellent mentor and friend to me, and has always provided me with wise advice during all these years. Professor Bhattacharya introduced me to the fascinating world of micromechanics during my first year at Caltech, which later turned out to be my research field, and I thank him for all the interesting discussions we have had.

I am indebted to my friend and former adviser Professor Juan Carlos de la Llera at Universidad Catolica de Chile for his mentorship and encouragement during the early years of my academic career. I am equally thankful to Professor Pedro Hidalgo for his friendship and support during my time in the industry. Dr. Nathan Barton

kindly hosted me during two summer internships at Lawrence Livermore National Laboratory, and I thank him for his guidance and friendship.

A special acknowledgement goes to my parents, Claudio and Ximena, and my siblings Jota, Gabriela, Pedro, Manuel and Caco, for their love, care and support. I am very proud of each one of them, and feel blessed to have such special and numerous family in Chile.

My experience at Caltech has been enjoyable due to the many good friends I have made over here. I would like to thank Lydia Suarez and Marta Kahl for their support and love all these years. My special appreciation goes to the former and present members of the Computational Solid Mechanics group I have met over the last four years.

The financial support of Conicyt Chile, the PSAAP center at Caltech and the Fulbright Commission in Chile is greatly appreciated.

Lastly, and more importantly, I am grateful to my wife Margarita for her unconditional love, care, support and patience. She always reminded me of what is truly important in life, making it much more enjoyable and meaningful. Our daughter Amanda made our time in Pasadena unique, bringing joy to our lives. It is to both of them I owe my mental sanity after all these fast-paced years at Caltech.

Abstract

Materials with micrometer dimensions and their distinct mechanical properties have generated a great interest in the material science community over the last couple of decades. There is strong experimental evidence showing that microcrystalline materials are capable of achieving much higher yield and fracture strength values than bulk mesoscopic samples as they decrease in size. Several theories have been proposed to explain the size effect found in micromaterials, but a predictive physics-based model suitable for numerical simulations remains an open avenue of research. Since the successful design of micro-electro-mechanical systems (MEMS) and novel engineered materials hinges upon the mechanical properties at the micrometer scale, there is a compelling need for a quantitative and accurate characterization of the size effects exhibited by metallic micromaterials.

This work is concerned with the multiscale material modeling and simulation of strength in crystalline materials with micrometer dimensions. The elasto-viscoplastic response is modeled using a continuum crystal plasticity formulation suitable for large-deformation problems. Crystallographic dislocation motion is accounted for by stating the crystal kinematics within the framework of continuously distributed

dislocation theory. The consideration of the dislocation self-energy and the step formation energy in the thermodynamic formulation of the constitutive relations renders the model non-local and introduces a length scale. Exploiting the concept of total variation we are able to recover an equivalent model that is local under a staggered approach, and therefore amenable to time integration using variational constitutive updates. Numerical simulations of compression tests in nickel micropillars using the proposed multiscale framework quantitatively capture the size dependence found in experimental results, showcasing the predictive capabilities of the model.

Contents

List of Figures

List of Tables

Chapter 1

Introduction

1.1 Motivation

Materials at the micrometer scale and their distinct properties have generated great interest in the material science community over the last couple of decades, leading to steady and intense research in this area. There is a vast amount of experimental evidence showing that microcrystalline materials are capable of achieving much higher yield and fracture strengths than the average values exhibited by bulk mesoscopic samples as they decrease in size. In particular, a prominent size-dependent effect was found in indentation tests on the surface of single crystals [86], torsion tests of Cu microwires [30], microbend tests of thin films[87], and more recently in compression tests of Ni [90], Au [36], Cu [48] and Al [66] micropillars. This size dependence is not found in bulk single crystals, where dimensions typically exceed 100μm. From an engineering design standpoint, these findings lead to the conclusion that in crystalline materials with sub-micrometer dimensions, the geometry and size become fundamental design parameters that strongly influence the strength of the material. Since the design of novel engineered materials and small devices like micro-electro-mechanical

systems (MEMS) rely upon the material mechanical properties, there is a great need for a quantitative and accurate characterization of the size effects exhibited by metallic micromaterials.

Size effects in metals have been known in physical metallurgy for more than half a century. In the case of polycrystalline materials, the yield strength shows a dependence on the grain size following the well-known Hall-Petch relation [39, 77], which was proposed in the early 1950s. This increase in strength through grain refinement has been largely exploited for industrial use, and the Hall-Petch relation has been verified for grains that range from millimeters to tens of nanometers [19]. By contrast, size effects in single crystals were considerably overlooked until the 1990s with the development of strain-gradient plasticity theories [27], despite the fact that they were reported in tension tests in Fe, Cu and Ag whiskers by Brenner in 1956 [14].

To date, the deformation mechanisms dictating the strength increase due to size decrease in microcrystals have not been fully understood [22, 68, 48]. Strain-gradient plasticity theories based on the concept of geometrically necessary dislocations and the ensuing crystal lattice curvature [27, 28] were successful in explaining the increase in strength resulting from inhomogeneous distribution of strain in torsion tests of whiskers [30] and indentation experiments in copper single crystals [67]. However, recent experiments in micropillars show large strength increases in the absence of significant gradients in the strain, limiting the applicability of strain-gradient theories

to fully explain these cases. Uchic et al. [90] attributed the increase in strength in single-slip Ni micropillars to the limitation of defect multiplication and storage as the sample diameter decreases. Greer, Oliver and Nix [36] found a similar trend in multislip compression tests of Au micropillars, which they explained using the concept of *dislocation starvation*. In the dislocation-starvation model, the diameter of the micropillar is assumed to be smaller than the length scale associated to dislocation multiplication by double cross-slip [34]. Then, dislocations will escape the crystal before dislocation breeding takes place, leaving the crystal dislocation-starved. High stresses are then needed to activate sources and nucleate new dislocations from the boundaries and interior, which would explain the observed high strength values.

In the search of a universal scaling law for the strength of crystalline micropillars, Dou and Derby [22] collected experimental data available in the literature on compression tests of micropillars. By setting the dislocation line tension as the controlling physical property and assuming an empirical power-law relation, they found a high correlation between the resolved shear stress normalized by the material shear modulus and the pillar diameter normalized by the Burgers vector magnitude for a variety of face-centered-cubic (FCC) metals (Ni, Au, Cu, Al), see Figure 1.1. This strong correlation corroborates the fact that dislocation motion and interaction with the sample geometry and physical dimensions influences the strength of micropillars, but does not clarify the mechanisms leading to the observed size-scale dependence.

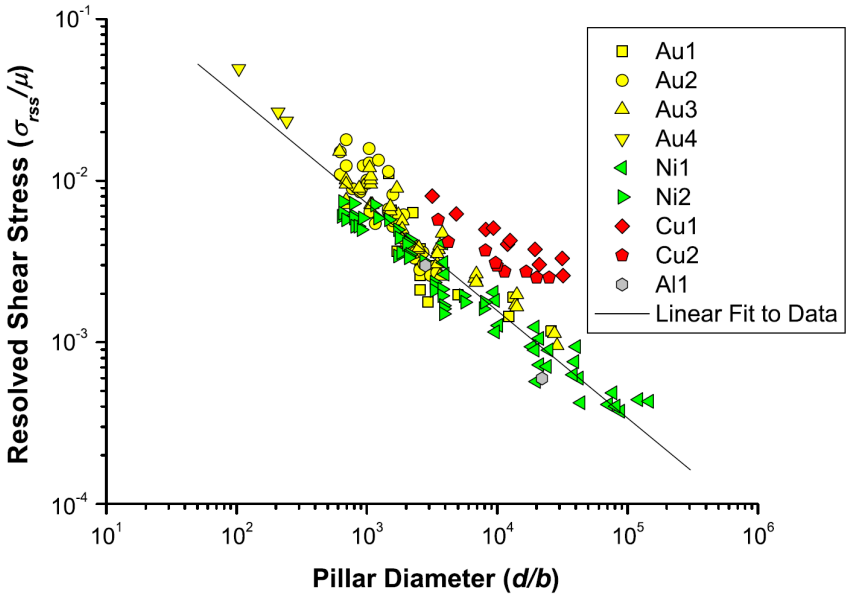

Figure 1.1: Strength dependence on the diameter in micropillar compression tests. Taken from [22].

Explanations of size effects in micropillars considering surface mechanisms have been considerably less explored. The FIB technique consists of Ga ion bombardment and necessarily implies ion implantation during the milling of the samples, thus affecting the chemical composition and mechanical properties of the surface. To investigate FIB surface damage, Kiener et al. [47] measured the Ga^+ concentration on Cu samples. The formation of an amorphous layer due to Ga^+ implantation was observed, with penetration depths up to 50 nm with concentrations of 20 at.% close to the sample surface, depending on the incidence angle, ion energy and ion dose. Figure 1.2 shows the grain surface of a polycrystalline copper sample partially exposed to ion bombardment, where the damaged surface can be clearly observed. Similar observations have been found for Au, Pt and W specimens [4, 58].

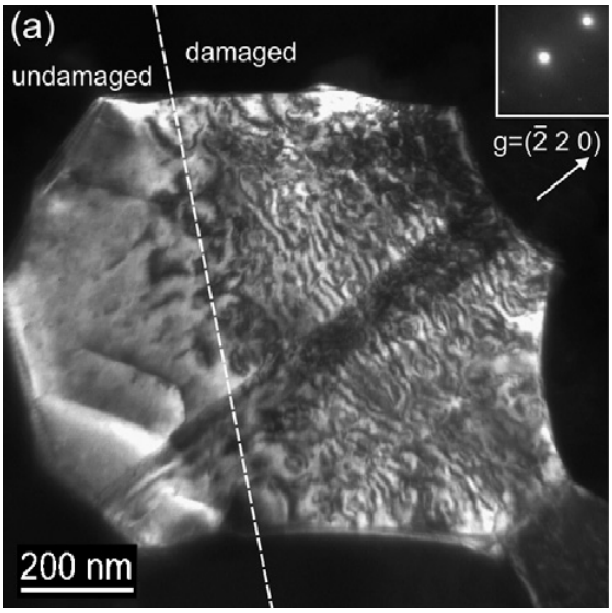

Figure 1.2: Dark-field TEM image of a Cu grain partially damaged by Ga^+ bombardment. Taken from [47].

1.2 Multiscale hierarchy in micron plasticity

Plasticity in metals is the product of complex mechanisms whose dependence and effects span several scales over length and time. Figure 1.3 shows the multiscale hierarchy encountered in micron plasticity. At its most fundamental level, the atomistic level represented by the left box in Figure 1.3, nucleation and motion of vacancies in the crystalline lattice generate defects that perturb the periodic lattice from its perfect configuration. Electronic calculations based on quantum mechanics have been able to describe the behavior of solids and formation and motion of defects at the atomic scale.

Aligned vacancies form line defects or *dislocations*, which can be observed as continuous lines in the sub-micrometer scale, as shown in the center picture of Figure 1.3.

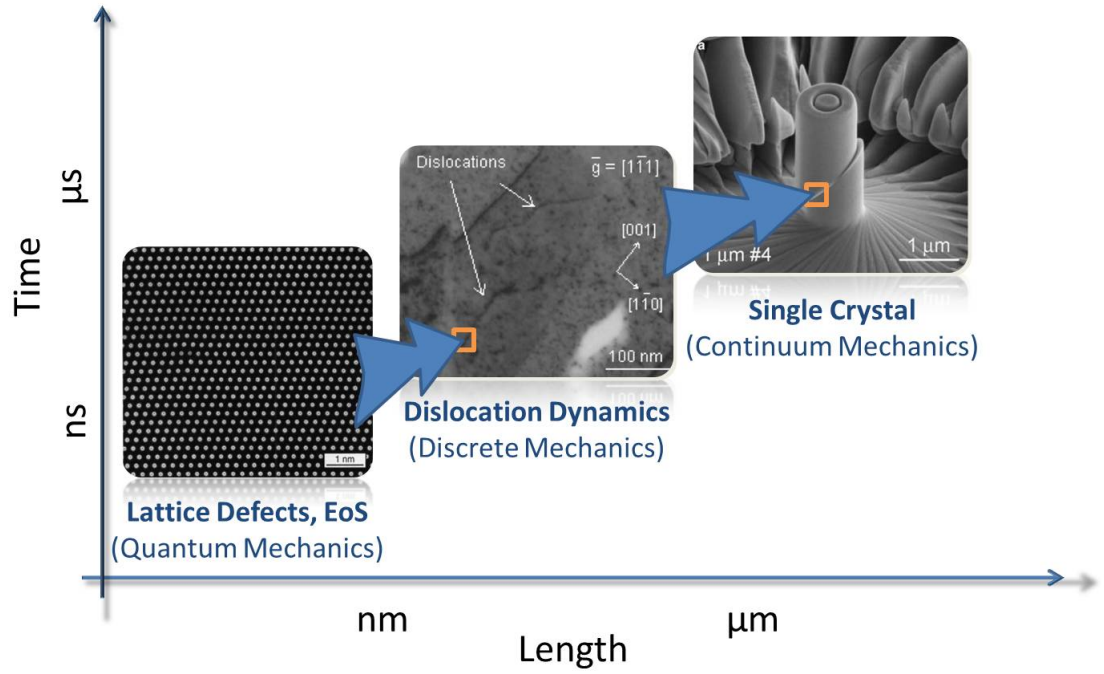

Figure 1.3: Multiscale hierarchy. Pictures taken from [35] and [21].

Dislocations are arguably the most important carrier of plasticity at this level, as we discuss next. The crystallographic nature of plasticity was first inferred by Ewing and Rosenhain in 1900 [25], from the observation of slip steps and slip bands on the surface of deformed metals that occur on crystallographic planes along crystallographic directions. Based on this observation, theoretical values for the shear strength were estimated by Frenkel in 1926 [32], which resulted in several orders of magnitude larger than the observed experimental values. These discrepancies were explained in 1934 by Taylor [88], Orowan [70] and Polanyi [78], who theorized about the existence of line defects, in the form of edge dislocations, which facilitated irreversible deformations in crystals, predicting strength values comparable to those found in experimental evidence. The existence of dislocations was only experimentally confirmed in 1953

by Vogel and co-workers [91], through the observation of pits after surface etching of germanium single crystals, a manifestation of the distortion caused to the perfect lattice distortion by crystallographic defects. Direct observations of dislocations were only possible later on with the invention of transmission electron microscopy (TEM).

Dislocations are represented in elasticity theory by discontinuities in the displacement field, and the standard treatise on dislocation theory is the book by Hirth and Lothe [44]. From a computational modeling standpoint, dislocation motion and the interaction of dislocation lines in a solid can be simulated using discrete dislocation dynamics (DDD) methods. The first simulations using DDD methods were developed by Lepinoux and Kubin [55], Amodeo and Ghoniem [2, 3] and Devincre and Condat [20].

If the length scale of interest is much greater than the characteristic length scale of the problem, i.e., interatomic distance, then a solid can be idealized as a continuum and, to a high accuracy, continuum mechanics predicts its mechanical behavior. This will be the working assumption of this work when modeling materials at the micrometer scale, as represented by the rightmost box in Figure 1.3. Besides its elegant mathematical description, continuum mechanics is amenable to computation using the finite element method, making a powerful tool for the analysis of problems in engineering and science. As pointed out by Needleman [64, 65], direct atomistic simulations and discrete dislocation dynamics simulations prove insightful

in the understanding of crystal plasticity. However, these methods are not viable for the simulation of micrometer-sized samples due to the intractable computational demands they impose. Therefore, the development of dislocation-based continuum crystal plasticity theories plays a crucial role in the feasibility of computational multiscale simulations.

1.3 Previous work in continuum crystal plasticity

The origins of continuum constitutive models for crystal plasticity date back to the seminal work of Taylor in 1938 [89], wherein a continuum model of slip was first considered. Hill [42] addressed the elastoplastic behavior of single crystals, and extended the work of Taylor to the context of linearized continuum mechanics. The generalization to finite kinematics was done by Rice [80], Kratochvil [50], Hill and Rice [43], Asaro and Rice [8] and Havner [41], among others. Traditional crystal plasticity models have been able to accurately represent the plastic response of single crystals with sub-milimeter dimensions. In particular, they all share the same *local* approach to crystal plasticity, in which hardening of the critical resolved shear stress depends directly on the slip, but not on its spatial gradients. It follows that traditional models are *scale invariant*, that is, they are unaffected by changes in the sample size.

As already mentioned in Section 1.2, it is widely accepted by the material science community that dislocation evolution is the most important mechanism responsible

for plastic deformations in crystals. This realization notwithstanding, the majority of the traditional crystal plasticity models do not explicitly account for the evolution of dislocation structures. Crystal plasticity models with a more direct consideration of dislocation evolution, in the form of continuous density measures, have been proposed only in the last twenty years, either by establishing a direct correspondence with the slip strain, as pursued by Cuitino and Ortiz [17, 18], or by directly considering the dislocation density as an internal variable itself, an approach taken by Arsenlis and Parks [5, 6]. Although these models introduce a length scale in the formulation, i.e., the magnitude of Burgers vector, they are local constitutive models, and therefore fall in the size-independent crystal plasticity category.

The origins of phenomenological strain-gradient plasticity theories date back to the work of Aifantis and co-workers [94, 62] on shear banding in metals. However, the connection of strain gradients with the continuum theory of dislocations was first made by Fleck and Hutchinson in 1993 [27], and further developed and validated in the work of Fleck et al. [30], where the size dependence of strength in copper wires under torsion was investigated. Fleck and co-workers considered a small-deformation setting, where the total dislocation density is decomposed into a geometrically necessary dislocations density (GND) and a statistically stored dislocations (SSD) density, as envisioned by Ashby in his landmark paper [9]. The GND density expresses the lattice incompatibility due to non-homogeneous plastic deformations, and its connection with continuum dislocation theory had been previously established in the 1960s

by Nye [69], Bilby et al. [12] and Kröner [51].

Since the establishment of strain-gradient theories, several developments based on the concept of GND density have been pursued. In the following, we mention some of the works that are relevant to this thesis. Acharya and Bassani [1] extended the theory to the framework of finite kinematics (see also [29]), and considered the hardening response of single crystals to depend on the dislocation density tensor, thus avoiding additional boundary conditions on the slip fields (see [65] for a discussion on the boundary value problems associated to different strain-gradient theories). Following a thermodynamic framework, Gurtin [37, 38] adds to the free energy density a defect energy, which depends on the GND density tensor, and further derives thermodynamic restrictions on the related constitutive models. Assuming a saturation dislocation density, Berdichevsky [10] proposes a simple phenomenological expression for the defect energy based on a scalar measure of the GND tensor, which is further used in the analytical solution of plane-constrained shear of a crystalline layer in single double slip by Le and Sembiring [52, 53].

1.4 Thesis outline

This thesis is organized as follows. Chapter 2 develops a finite-kinematics non-local plasticity model for general elasto-viscoplastic crystalline materials. The continuously-distributed dislocation theory is reviewed, together with its connection with the kine-

matics of single crystals. Following a thermodynamic framework, the free-energy density and dissipation potential are introduced along with their corresponding expressions for crystalline materials. In particular, the crystal defect free-energy term is obtained by appealing to the dislocation self-energy, which introduces strain gradients in the formulation. The concept of total variation is then exploited to recover an equivalent expression for the dislocation self-energy based on the slip field alone. Surface free energy resulting from step formation is considered in the model by using a simple geometrical construction based on the slip strain field.

The numerical implementation of the crystal plasticity model is the focus of Chapter 3. By considering a staggered approach, it is shown that the proposed crystal plasticity model becomes local, and therefore amenable to variational constitutive updates. A novel flow-rule update based on the theory of differential manifolds is presented along with comparison against updates using the computationally more expensive exponential map. The spatial integration of the model is addressed by means of the finite element method, where near-incompressibility issues are tackled using a finite-kinematics extension of the mean-dilatation formulation. Computational aspects and the parallel implementation of the proposed numerical method are presented.

In Chapter 4, the proposed model is demonstrated by numerical simulations of nickel micropillars compression tests. In particular, stress-strain curves for several

micropillar diameters and its comparison with experimental results are presented. The simulated values for strength are represented by a fitted power-law expression, and compared to results found in the literature.

Finally, we present the conclusions from this work along with possible future directions in Chapter 5.

Chapter 2

Theoretical framework

2.1 Dislocation theory

Dislocation theory plays an important role in understanding plastic processes at the micro- and nano-meter scales. From a material science point of view, a dislocation is a crystallographic defect, and a dislocation line defines the boundary between two "perfect" parts of a crystal lattice. Dislocations have been observed experimentally, and they explain plastic slip in crystals. Furthermore, dislocations are responsible for the formation of microstructure in materials. Elasticity theory has been successfully applied to quantitatively model dislocations in solids, and has proven to be a predictive tool in the mechanical behavior of materials.

2.1.1 Continuously-distributed dislocation theory

Consider an element of oriented differential area $\boldsymbol{n}dS$ with dislocation lines threading it, as shown in Figure 2.1. Let $d\boldsymbol{b}$ be the Burgers vector resulting from all dislocations threading dS. Taking a continuum perspective we assume that dislocations are *continuously distributed* in the sense that there exists a Burgers vector area density

$\boldsymbol{c}$ such that the resulting Burgers vector for a differential area can be expressed as

$$\mathrm{d}\boldsymbol{b} = \boldsymbol{c}\,\mathrm{d}S \tag{2.1}$$

Integration over a finite surface S yields the total Burger vector

$$\boldsymbol{b}(S) = \int_S \mathrm{d}\boldsymbol{b} = \int_S \boldsymbol{c}\,\mathrm{d}S \tag{2.2}$$

Since dislocation lines cannot end inside the volume that contains them, we have that for a closed surface S_c

$$\boldsymbol{b}(S_c) = \int_{S_c} \boldsymbol{c}\,\mathrm{d}S_c = 0 \tag{2.3}$$

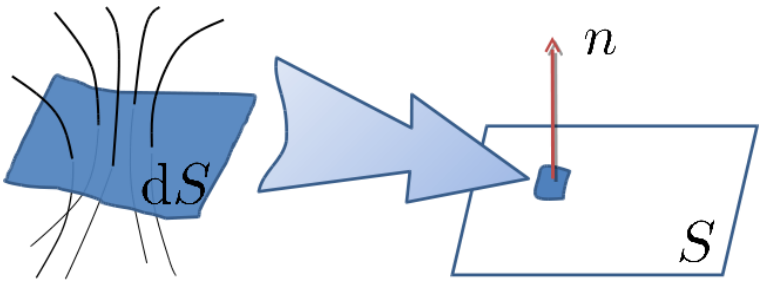

Figure 2.1: Continuous distribution of dislocations.

Now consider the case of a tetrahedron, whose surface is closed. Using the previous result and following an argument similar to that of the Cauchy's tetrahedron theorem, it can be shown that the area density $\boldsymbol{c}$ depends linearly on the normal to the differential area

$$\boldsymbol{c}(\boldsymbol{n}) = \mathsf{A}\,\boldsymbol{n} \tag{2.4}$$

where A is defined as the *dislocation-density tensor* [69]. Therefore we can rewrite

2.2 as

$$\boldsymbol{b}(S) = \int_S \mathsf{A}\,\boldsymbol{n}\,\mathrm{d}S \tag{2.5}$$

It is important to remark that, in representing the behavior of individual dislocation lines by a continuously distributed measure, some individual dislocation information is lost. For example, if the differential volume being represented by Nye's tensor contains dislocations dipoles only,[1] then the net Nye's tensor is zero since the resulting Burgers vector is zero. Dislocation dipoles, along with other redundant structures like planar dislocation loops fully contained in the represented volume, do not contribute to the GND tensor, and are considered statistically-stored dislocations (SSD) [5]. We conclude that the continuous representation of dislocations by the Nye tensor only considers non-redundant dislocation structures, which relate to strain-gradient fields, as we explain in section 2.2.1.

We now relate the concept of dislocation-density tensor with continuum measures of deformation. Consider for simplicity a linearized-kinematics framework, where the total displacement field $\boldsymbol{u} : \Omega \to \mathbb{R}^3$ defines the deformation in a solid occupying a domain Ω. Further, assume $\boldsymbol{u} \in C^1$. A standard decomposition of the total

[1] A dislocation dipole is a pair of dislocations whose directions are parallel, but Burgers vectors are opposite.

displacement gradient reads

$$\nabla \boldsymbol{u} = \frac{\partial \boldsymbol{u}}{\partial \boldsymbol{X}} = \boldsymbol{\beta}^e + \boldsymbol{\beta}^p \tag{2.6}$$

where $\boldsymbol{\beta}^e$ is the elastic displacement gradient associated with reversible crystal deformations, and $\boldsymbol{\beta}^p$ is the plastic displacement gradient (plastic distortion), which we associate with plastic deformations due to dislocation motion.

From continuum mechanics, we require the total displacement gradient $\nabla \boldsymbol{u}$ to satisfy compatibility conditions. However, neither the plastic nor the elastic displacement gradients are subject to any such requirement. In fact, the incompatibility of $\boldsymbol{\beta}^p$ is related to dislocations within the crystal and, in turn, to the dislocation density tensor as we show next. Let Γ be a smooth closed circuit in the undeformed crystal, otherwise known as the Burgers circuit. From the incompatibility of $\boldsymbol{\beta}^p$ we will generally obtain a non-zero Burgers vector

$$\boldsymbol{b}(\Gamma) = \oint_{\Gamma} \boldsymbol{\beta}^p \, d\boldsymbol{X} \tag{2.7}$$

which equals to the sum of the Burgers vectors for all dislocations encircled by Γ. Let S be a smooth surface whose boundary is Γ. Then, by Stokes theorem we have

$$\boldsymbol{b}(S) = \int_S (\boldsymbol{\beta}^p \times \nabla) \, \boldsymbol{n} \, \mathrm{d}S \tag{2.8}$$

Comparing 2.8 to 2.5 we conclude that

$$\mathsf{A} = \boldsymbol{\beta}^p \times \nabla \tag{2.9}$$

which defines the relation between the dislocation density tensor and the plastic distortion tensor. A direct consequence of 2.9 is the divergence-free property of the dislocation density tensor

$$\mathsf{A} \cdot \nabla = 0 \tag{2.10}$$

which embodies the physical requirement that dislocation lines cannot end in the interior of the body. Identity 2.10 also represents the conservation of Burgers vector or *Frank's rule*.

Following Ortiz and Repetto [74], we consider the case of a dislocation loop C contained in a plane with normal $\boldsymbol{m}$, a configuration typically encountered in crystalline materials, where slip occurs on discrete crystallographic planes. The corresponding dislocation density tensor is

$$\mathsf{A}(\boldsymbol{X}) = \boldsymbol{b} \otimes \boldsymbol{t}(\boldsymbol{X})\, \delta_C(\boldsymbol{X}) \tag{2.11}$$

where $\boldsymbol{b}$ is the Burgers vector of the dislocation, $\boldsymbol{t}$ is the unit tangent to C and δ_C is the Dirac delta supported on C. Then, the dislocation length contained in the volume

Ω is

$$L = \int_{\Omega} \frac{\|\mathsf{A}\|_F}{|\boldsymbol{b}|}\, dV \tag{2.12}$$

where $\|\cdot\|_F$ is the Frobenius norm, and $|\boldsymbol{b}|$ is the Burgers vector magnitude.

2.1.2 Self-energy of a dislocation line

Dislocations are represented in elasticity theory by discontinuities in the displacement field, which render the displacement gradient incompatible. A dislocation line generates a stress field within the solid that contains it. We define the *dislocation self-energy* as the strain energy resulting from the stress field induced by a dislocation in a solid.

Example 1. *Consider a screw dislocation with Burgers vector b_z contained in a hollow cylinder of length L, outer radius R and inner radius r_0. From elasticity theory the dislocation self-energy per unit length is*

$$\frac{E^{\text{self}}_{\text{screw}}}{L} = \frac{\mu b_z^2}{4\pi} \ln \frac{R}{r_0} \tag{2.13}$$

where μ is the elastic shear modulus. For the case of an edge dislocation with Burgers vector b_x we have that the self energy is

$$\frac{E^{\text{self}}_{\text{edge}}}{L} = \frac{\mu b_x^2}{4\pi(1-\nu)} \ln \frac{R}{r_0} \tag{2.14}$$

where ν is the Poisson ratio. [44]

In general dislocations have a mixed character, which can be decomposed into edge and screw components. This yields a self-energy that is a superposition of both edge and screw energies, with appropriate values for the corresponding Burgers vectors. A simple analysis using realistic values for R and r_0 yields the general expression for the self-energy of a mixed dislocation per unit length

$$\frac{E^{\text{self}}_{\text{mixed}}}{L} = \alpha\mu b^2 \tag{2.15}$$

where α is of the order of unity.

From 2.15 we observe that the strain energy of a mixed dislocation is proportional to its length, and therefore an increase in length results in an increase in strain energy. This observation brings the concept of *line tension*, which is defined as the increase in strain energy per unit increase in the length of a dislocation line. Thus, 2.15 can be seen as the expression for the line tension T

$$T = \alpha\mu b^2 \tag{2.16}$$

In writing 2.16 we have assumed that T is independent of the orientation of the dislocation segment, i.e., we consider it an isotropic line tension.

In particular, and within the context of continuously distributed dislocations, we

can use 2.12 to estimate the total dislocation length contained in a volume Ω. Assume further that α takes a constant representative value in Ω, then the total dislocation self-energy in a crystal can be expressed as

$$E^{\text{self}} = TL = \int_{\Omega} \frac{T\|\mathsf{A}\|_F}{|\boldsymbol{b}|}\, dV \tag{2.17}$$

and the dislocation self-energy density reads

$$W^{\text{self}} = \frac{T\|\mathsf{A}\|_F}{|\boldsymbol{b}|} \tag{2.18}$$

2.2 Non-local continuum single crystal plasticity

Thermodynamics furnishes a general and complete framework to develop constitutive material models. In this section, we identify the fields that describe the material thermodynamic state, and postulate the thermodynamic potentials that relate these fields with the physical governing laws. For a complete discussion of continuum mechanics, see references [59] and [7].

2.2.1 Kinematics of crystal plasticity

Consider a crystalline body occupying a domain $\Omega \subset \mathbb{R}^3$ in its reference configuration, which we assume to be stress free at time $t = t_1$. We adopt a Lagrangian description for the kinematics of the crystal, and represent the motion from the reference to the current configuration by the *deformation mapping* $\boldsymbol{\varphi} \in C^1(\Omega \times [t_1, t_2], \mathbb{R}^3)$. A

standard measure of deformation is the *deformation gradient*

$$\boldsymbol{F}(\boldsymbol{X},t) := \frac{\partial \boldsymbol{\varphi}(\boldsymbol{X},\boldsymbol{t})}{\partial \boldsymbol{X}} \qquad \boldsymbol{X} \in \Omega \tag{2.19}$$

A measure of the volumetric change of an infinitesimal volume element in the solid is given by the Jacobian $J : \Omega \times [t_1, t_2] \to \mathbb{R}$, defined by

$$J(\boldsymbol{X},t) := \det(\boldsymbol{F}(\boldsymbol{X},t)) \tag{2.20}$$

where $\det : \mathbb{R}^{3\times 3} \to \mathbb{R}$ is the determinant mapping. For the sake of clarity, we drop the arguments of functions in the sequel. Assuming the crystal deformation consists of plastic deformations produced by dislocation motion, and elastic deformations are associated to reversible distortion of the lattice, we consider the multiplicative decomposition of the deformation gradient $\boldsymbol{F}$ into an elastic deformation gradient $\boldsymbol{F}^e$ and a plastic deformation gradient $\boldsymbol{F}^p$, as proposed by Lee [54],

$$\boldsymbol{F} = \boldsymbol{F}^p \boldsymbol{F}^e \tag{2.21}$$

Following Asaro and Rice [8], we further assume that $\boldsymbol{F}^p$ maps the crystal reference configuration Ω to an *intermediate configuration* Ω^p where only crystallographic slip occurs, leaving the crystal lattice unrotated and undistorted. In particular, there are no volume changes associated with plastic deformations in incompressible plasticity,

i.e., the plastic deformation gradient satisfies the condition

$$\det(\boldsymbol{F}^p) = 1 \tag{2.22}$$

The rotation and distortion of the lattice are described by the elastic deformation gradient $\boldsymbol{F}^e$, which maps the body in the intermediate configuration into the current configuration. This choice of kinematics uniquely determines the multiplicative decomposition 2.21.

The evolution of the plastic deformation gradient is governed by the flow rule

$$\dot{\boldsymbol{F}}^p = \boldsymbol{L}^p \boldsymbol{F}^p \tag{2.23}$$

where $\boldsymbol{L}^p$ is the plastic velocity gradient. It is customary in crystal plasticity to assume that plastic deformations are the result of slip due to dislocation motion along particular crystallographic systems, defined by the pair $(\boldsymbol{m}^\alpha, \boldsymbol{s}^\alpha)$: the plane normal and Burgers vector direction, respectively, of the α-slip system in the intermediate or undistorted lattice configuration. Since the Burgers vector $\boldsymbol{s}^\alpha$ is contained in the plane defined by $\boldsymbol{m}^{\boldsymbol{\alpha}}$, it follows from orthogonality that

$$\boldsymbol{s}^\alpha \cdot \boldsymbol{m}^\alpha = 0 \tag{2.24}$$

For the case of face-centered-cubic crystal structure, the slip systems are detailed in

Table 2.1. Since the crystal lattice in the intermediate configuration remains undistorted, these vectors are assumed constant throughout the crystal motion. Rice [80] proposed an expression for the plastic velocity gradient based on the superposition of the slip-system contributions

$$\boldsymbol{L}^p = \sum_{\alpha=1}^{N} \dot{\gamma}^\alpha \boldsymbol{s}^\alpha \otimes \boldsymbol{m}^\alpha \tag{2.25}$$

where $\gamma^\alpha : \Omega \times [t_1, t_2] \to \mathbb{R}$, $\alpha = 1, \ldots, N$ are the slip strain fields, or simply *slip fields*. For convenience, we define the collection of slip fields by the vector $\boldsymbol{\gamma} : \Omega \times [t_1, t_2] \to \mathbb{R}^N$, and assume initial conditions for the slip fields given by

$$\boldsymbol{\gamma}(\boldsymbol{X}, t_1) = \boldsymbol{\gamma}_0(\boldsymbol{X}) \qquad , \qquad \boldsymbol{X} \in \Omega \tag{2.26}$$

The choice of crystallographic slip as the measure of irreversible deformations naturally defines them as internal variables. Moreover, plastic irreversibility requires that

$$\dot{\gamma}^\alpha \geq 0 \qquad \alpha = 1, \ldots, N \tag{2.27}$$

It follows from the orthogonality condition 2.24 that

$$\operatorname{trace}(\boldsymbol{L}^p) = 0 \tag{2.28}$$

i.e., the evolution of plastic deformations governed by 2.25 conforms to the incompressibility condition of plastic processes, as evidenced by experimental observations.

Expression 2.25 together with 2.23 yields the *crystallographic flow rule*

$$\dot{\boldsymbol{F}}^p = \left(\sum_{\alpha=1}^{N} \dot{\gamma}^\alpha \boldsymbol{s}^\alpha \otimes \boldsymbol{m}^\alpha \right) \boldsymbol{F}^p \tag{2.29}$$

Equation 2.31 describe the evolution of the plastic deformation gradient in terms of the slip fields, and thus represents a non-holonomic constraint implicitly relating $\boldsymbol{\gamma}$ and $\boldsymbol{F}^p$.

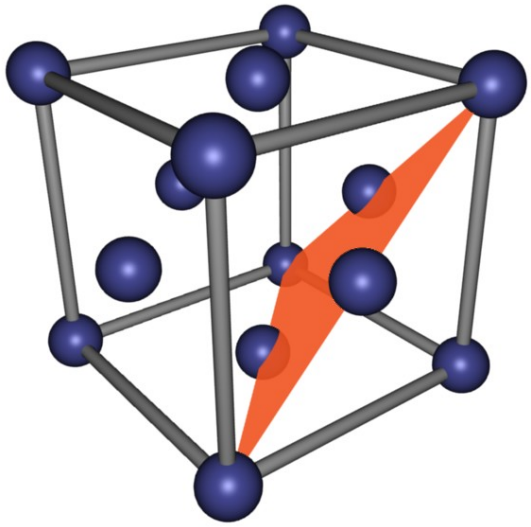

Figure 2.2: FCC atomic structure and {111} slip plane.

Next, we establish a connection between the continuous description of dislocation motion and crystal kinematics. Let the deviation from the undeformed configuration be described by a small *displacement field* $\boldsymbol{u} \in C^1(\Omega \times [t_1, t_2], \mathbb{R}^3)$, such that $\boldsymbol{\varphi} = \boldsymbol{I} + \boldsymbol{u}$. Then, the linearization of 2.21 about Ω in the direction of the displacement field yields

$$\nabla \boldsymbol{u} = \boldsymbol{\beta} = \boldsymbol{\beta}^e + \boldsymbol{\beta}^p \tag{2.30}$$

Slip System	Plane Normal $\boldsymbol{m}^\alpha$	Slip Direction $\boldsymbol{s}^\alpha$
A2	$(\bar{1}11)$	$\pm[01\bar{1}]$
A3	$(\bar{1}11)$	$\pm[101]$
A6	$(\bar{1}11)$	$\pm[110]$
B2	(111)	$\pm[01\bar{1}]$
B4	(111)	$\pm[10\bar{1}]$
B5	(111)	$\pm[\bar{1}10]$
C1	$(\bar{1}\bar{1}1)$	$\pm[011]$
C3	$(\bar{1}\bar{1}1)$	$\pm[101]$
C5	$(\bar{1}\bar{1}1)$	$\pm[\bar{1}10]$
D1	$(1\bar{1}1)$	$\pm[011]$
D4	$(1\bar{1}1)$	$\pm[10\bar{1}]$
D6	$(1\bar{1}1)$	$\pm[110]$

Table 2.1: Slip systems for FCC crystals.

where $\boldsymbol{\beta}^e$ is the elastic displacement gradient, and $\boldsymbol{\beta}^p$ is the inelastic displacement gradient, also known as the *plastic distortion tensor*. Noting that the linearization of $\boldsymbol{L}^p$ is $\dot{\boldsymbol{\beta}}^p$, we can directly integrate the linearized version of flow rule 2.25 to obtain

$$\boldsymbol{\beta}^p = \sum_{\alpha=1}^{N} \gamma^\alpha \boldsymbol{s}^\alpha \otimes \boldsymbol{m}^\alpha \tag{2.31}$$

At this point, a connection between the continuously-distributed dislocation theory and the crystal continuum kinematics is readily made. We associate slip in each crystallographic system α with the conservative motion of dislocations in the crystal plane defined by $\boldsymbol{m}^\alpha$ and having total Burgers vector with direction $\boldsymbol{s}^\alpha$. Moreover, for each such crystallographic system we define the *slip-system dislocation tensor* A^α

from Kroner's relation 2.9,

$$\mathsf{A}^\alpha = \boldsymbol{s}^\alpha \otimes (\nabla\gamma^\alpha \times \boldsymbol{m}^\alpha) \tag{2.32}$$

From 2.12, the total dislocation length corresponding to the α-system is computed by

$$L^\alpha = \int_\Omega \frac{\|\boldsymbol{s}^\alpha \otimes (\nabla\gamma^\alpha \times \boldsymbol{m}^\alpha)\,\|_F}{|b|}\,\mathrm{d}x \tag{2.33}$$

which, after some algebra (see Appendix B) reduces to

$$L^\alpha = \int_\Omega \frac{\|\nabla_{\mathcal{P}^\alpha}\gamma^\alpha\|_2}{|b|}\,\mathrm{d}x \tag{2.34}$$

where the norm $\|\cdot\|_2 : \mathbb{R}^3 \to \mathbb{R}$ used in the last expression denotes the Euclidean norm, and

$$\nabla_{\mathcal{P}^\alpha}\gamma^\alpha := \mathcal{P}^\alpha\,\nabla\gamma^\alpha \tag{2.35}$$

is the *slip in-plane gradient* where

$$\mathcal{P}^\alpha := \boldsymbol{I} - \boldsymbol{m}^\alpha \otimes \boldsymbol{m}^\alpha \tag{2.36}$$

is the *orthogonal-projection operator* onto the plane defined by the normal $\boldsymbol{m}^\alpha$.

2.2.2 Conservation laws

The motion of a solid is governed by conservation laws. In the following, we consider a solid deforming under quasi-static conditions, and neglect inertial terms in the statement of balance equations. All balance equations are expressed in *Lagrangian form*, that is, with respect to the reference configuration. Let $\mathcal{S} \subset \Omega$ be an arbitrary sub-body and $\partial\mathcal{S}$ be the sub-body boundary, and let $\rho_0 : \Omega \times [t_1, t_2] \to \mathbb{R}$ be the mass density per unit undeformed volume. The *conservation of mass* requires that

$$\frac{\mathrm{d}}{\mathrm{d}t} \int_{\mathcal{S}} \rho_0 \, \mathrm{d}V = \int_{\mathcal{S}} \dot{\rho}_0 \, \mathrm{d}V = 0 \tag{2.37}$$

where the first equality is obtained by noting that $\mathcal{S}$ does not change in time. Since $\mathcal{S}$ is arbitrary, a necessary condition for 2.37 to hold is that the integrand equal zero, that is

$$\dot{\rho}_0 = 0 \qquad \text{in } \Omega \tag{2.38}$$

which is also known as the *local form of mass conservation*.

Let $\boldsymbol{B} : \Omega \times [t_1, t_2] \to \mathbb{R}^3$ be the body forces per unit mass, and $\boldsymbol{T} : \Omega \times [t_1, t_2] \to \mathbb{R}^3$ be the tractions per unit undeformed area. Then, the *conservation of linear momentum* reads

$$\int_{\mathcal{S}} \rho_0 \, \boldsymbol{B} \, \mathrm{d}V + \int_{\partial\mathcal{S}} \boldsymbol{T} \, \mathrm{d}S = 0 \tag{2.39}$$

Cauchy's tetrahedron theorem in material form states that

$$\boldsymbol{T} = \boldsymbol{P}\boldsymbol{N} \tag{2.40}$$

where $\boldsymbol{P} : \Omega \times [t_1, t_2] \to \mathbb{R}^{3\times 3}$ is the first Piola-Kirchhoff tensor and $\boldsymbol{N} : \Omega \to \mathbb{R}^3$ is the boundary unit outward normal. Thus, equation 2.39 takes the form

$$\int_{\mathcal{S}} \rho_0 \, \boldsymbol{B} \, \mathrm{d}V + \int_{\partial\mathcal{S}} \boldsymbol{P}\boldsymbol{N} \, \mathrm{d}S = 0 \tag{2.41}$$

An application of the divergence theorem on the surface integral of 2.41, together with the arbitrariness of $\mathcal{S}$, yields the local form for the balance of linear momentum

$$\nabla \cdot \boldsymbol{P} + \rho_0 \, \boldsymbol{B} = 0 \qquad \text{in } \Omega \tag{2.42}$$

which is otherwise known as *mechanical equilibrium*. Finally, the *conservation of angular momentum* states that

$$\int_{\mathcal{S}} \boldsymbol{\varphi} \times (\rho_0 \, \boldsymbol{B}) \, \mathrm{d}V + \int_{\partial\mathcal{S}} \boldsymbol{\varphi} \times (\boldsymbol{P}\,\boldsymbol{N}) \, \mathrm{d}S = 0 \tag{2.43}$$

which can be shown to take the local form

$$\boldsymbol{P}\boldsymbol{F}^T = \boldsymbol{F}\boldsymbol{P} \tag{2.44}$$

Since the Cauchy stress tensor is related to the first Piola-Kirchhoff tensor through

the relation

$$\boldsymbol{\sigma} = J^{-1}\boldsymbol{P}\boldsymbol{F}^{-T} \tag{2.45}$$

we conclude that the conservation of angular momentum implies the symmetry of the Cachy stress tensor, i.e.,

$$\boldsymbol{\sigma} = \boldsymbol{\sigma}^{T} \tag{2.46}$$

The governing equations obtained from conservation laws should be furnished with initial and boundary conditions. We assume initial conditions for the deformation mapping of the form

$$\boldsymbol{\varphi}(\boldsymbol{X}, t_1) = \boldsymbol{\varphi}_0(\boldsymbol{X}) \qquad , \qquad \boldsymbol{X} \in \Omega \tag{2.47}$$

The domain boundary $\partial\Omega$ is assumed to be the disjoint union of the *displacement boundary* $\partial\Omega_1$, where essential or Dirichlet boundary conditions follow from the prescription of the displacement field, i.e.,

$$\boldsymbol{\varphi} = \bar{\boldsymbol{\varphi}} \qquad \text{on } \partial\Omega_1 \tag{2.48}$$

and the *traction boundary* $\partial\Omega_2$, where natural or Neumann boundary conditions take the form

$$\boldsymbol{P}\,\boldsymbol{N} = \bar{\boldsymbol{T}} \qquad \text{on } \partial\Omega_2 \tag{2.49}$$

where $\bar{\boldsymbol{T}} : \partial\Omega_2 \times [t_1, t_2] \to \mathbb{R}^3$ are the prescribed tractions.

2.2.3 Thermodynamic formalism and constitutive formulation

Having identified the fields that represent the kinematics of the problem and their connection with the theory of continuously-distributed dislocations, together with the conservation laws that govern the motion of the solid, we are ready to develop the constitutive model. In this work, we follow an internal-variable thermodynamic framework [56, 57], which governs irreversible processes in solids, and identify the slip fields $\boldsymbol{\gamma}$ as the natural internal variables for crystalline materials. An extension of this thermodynamic formalism to the non-local case, where internal processes depend on the derivatives of the internal variables, is presented in [11]. Throughout this work we consider only isothermal processes, and thus omit the dependence of the material model on temperature, and conversion of plastic work into heat thereof. An extension of the thermodynamic internal-variable formalism that addresses the conversion of plastic work into heat was developed by Rosakis et al. [81].

We start our discussion by postulating the existence of an internal energy $E_{\mathcal{S}}$ stored in a sub-body $\mathcal{S} \subset \Omega$ of the solid, which depends on the kinematic fields describing the motion of the solid, internal variables governing irreversible processes, and the specific entropy $\eta : \Omega \to \mathbb{R}$, which is a measure of the microstructural disorder of the system. We distinguish between bulk and boundary surface contributions to

the internal energy of the sub-body, and write

$$E_{\mathcal{S}} = E_{\mathcal{S}}^{\text{bulk}} + E_{\mathcal{S}}^{\text{surf}} \tag{2.50}$$

The bulk component of the internal energy can be expressed in terms of a internal energy density per unit undeformed volume e integrated over the sub-body domain

$$E_{\mathcal{S}}^{\text{bulk}} = \int_{\mathcal{S}} e(\boldsymbol{F}, \boldsymbol{\gamma}, \nabla\boldsymbol{\gamma}, \eta)\, \mathrm{d}V \tag{2.51}$$

while the surface energy is assumed to have the form

$$E_{\mathcal{S}}^{\text{surf}} = \int_{\partial\mathcal{S}\cap\partial\Omega} \Pi(\boldsymbol{\gamma})\, \mathrm{d}S \tag{2.52}$$

where Π is the energy per unit undeformed area associated with the creation of new surfaces at the boundary of the solid. We remark that in writing 2.52, we have implied that if $\partial\mathcal{S}\cap\partial\Omega = \emptyset$, then $E_{\mathcal{S}}^{\text{surf}} = 0$. The implicit assumption that the bulk and surface energy densities depend on $(\boldsymbol{F}, \boldsymbol{\gamma}, \nabla\boldsymbol{\gamma})$ and $\boldsymbol{\gamma}$, respectively, will be justified later during their explicit formulation.

The power of the body forces and tractions applied to $\mathcal{S}$, or *external power*, is

defined as

$$\begin{aligned} P_{\mathcal{S}} &= \int_{\mathcal{S}} \rho_0 \boldsymbol{B} \cdot \dot{\boldsymbol{\varphi}} \, \mathrm{d}V + \int_{\partial\mathcal{S}} \boldsymbol{T} \cdot \dot{\boldsymbol{\varphi}} \, \mathrm{d}S \\ &= \int_{\mathcal{S}} \rho_0 \boldsymbol{B} \cdot \dot{\boldsymbol{\varphi}} \, \mathrm{d}V + \int_{\partial\mathcal{S}} \dot{\boldsymbol{\varphi}} \cdot \boldsymbol{P}\boldsymbol{N} \, \mathrm{d}S \end{aligned} \tag{2.53}$$

The first law of thermodynamics states that, in the absence of heat fluxes, the internal energy rate in a sub-body $\mathcal{S}$ equals the external power,

$$\frac{\mathrm{d}}{\mathrm{d}t} E_{\mathcal{S}} = P_{\mathcal{S}} \tag{2.54}$$

Using the divergence theorem to transform the surface integral in 2.53, conservation of linear momentum and integration by parts, we arrive at an equivalent statement of the first law of thermodynamics given by

$$\begin{aligned} \int_{\mathcal{S}} \left[\frac{\partial e}{\partial \eta} \, \dot{\eta} + \left(\frac{\partial e}{\partial \boldsymbol{F}} - \boldsymbol{P} \right) : \dot{\boldsymbol{F}} + \sum_{\alpha} \left(\frac{\partial e}{\partial \gamma^{\alpha}} - \nabla \cdot \frac{\partial e}{\partial \nabla \gamma^{\alpha}} \right) \dot{\gamma}^{\alpha} \right] \mathrm{d}V + \\ \int_{\partial\mathcal{S} \cap \partial\Omega} \sum_{\alpha} \left(\frac{\partial e}{\partial \nabla \gamma^{\alpha}} \cdot \boldsymbol{N} + \frac{\partial \Pi}{\partial \gamma^{\alpha}} \right) \dot{\gamma}^{\alpha} \, \mathrm{d}S = 0 \end{aligned} \tag{2.55}$$

where we define the *absolute temperature* by

$$\theta := \frac{\partial e}{\partial \eta} \tag{2.56}$$

Since the sub-body $\mathcal{S}$ is arbitrary, the integrands in 2.55 must be identically zero.

From the volumetric term we obtain

$$\theta\,\dot{\eta} = -\left(\frac{\partial e}{\partial \boldsymbol{F}} - \boldsymbol{P}\right) : \dot{\boldsymbol{F}} + \sum_{\alpha} -\left(\frac{\partial e}{\partial \gamma^{\alpha}} - \nabla \cdot \frac{\partial e}{\partial \nabla \gamma^{\alpha}}\right)\dot{\gamma}^{\alpha} \tag{2.57}$$

from which we identify the thermodynamic forces conjugate to the internal variables, or *driving forces*, by

$$\tau^{\alpha} := -\left(\frac{\partial e}{\partial \gamma^{\alpha}} - \nabla \cdot \frac{\partial e}{\partial \nabla \gamma^{\alpha}}\right) = -\frac{\delta e}{\delta \gamma^{\alpha}} \qquad \alpha = 1, \ldots, N \tag{2.58}$$

where $\dfrac{\delta e}{\delta \gamma^{\alpha}}$ means the variational derivative of the internal energy. Since the internal energy density and surface energy density do not depend directly on the slip strain rate, it follows that a necessary condition for the surface integral in 2.55 to be zero is

$$\frac{\partial e}{\partial \nabla \gamma^{\alpha}} \cdot \boldsymbol{N} + \frac{\partial \Pi}{\partial \gamma^{\alpha}} = 0 \qquad \text{on } \partial\Omega \quad , \alpha = 1, \ldots, N \tag{2.59}$$

which, as it will be apparent later on, provides boundary conditions for the slip fields.

The second law of thermodynamics requires the entropy rate to be positive, which reads

$$\theta\dot{\eta} = -\left(\frac{\partial e}{\partial \boldsymbol{F}} - \boldsymbol{P}\right) : \dot{\boldsymbol{F}} + \sum_{\alpha} \tau^{\alpha}\dot{\gamma}^{\alpha} \geq 0 \tag{2.60}$$

In the sequel, we denote $\boldsymbol{\tau} = [\tau^1, \ldots, \tau^N]$ the vector of driving forces. In order for

the inequality 2.60 to remain valid for all $\dot{\boldsymbol{F}}$, we require that

$$\boldsymbol{P} = \frac{\partial e}{\partial \boldsymbol{F}} \tag{2.61}$$

which is the well-known Coleman relation. Therefore, the second law of thermodynamics imposes the following constraint on the driving forces,

$$\sum_{\alpha} \tau^{\alpha} \dot{\gamma}^{\alpha} = \boldsymbol{\tau} \cdot \dot{\boldsymbol{\gamma}} \geq 0 \tag{2.62}$$

which is also known as the *reduced dissipation inequality*.

The importance of the internal energy density in the constitutive formulation of materials is clear from the foregoing developments. Alternatively, one may introduce the Helmholtz free-energy density by recourse to the Legendre transform

$$A(\boldsymbol{F}, \boldsymbol{\gamma}, \nabla\boldsymbol{\gamma}, \theta) := \inf_{\eta} \left[e(\boldsymbol{F}, \boldsymbol{\gamma}, \nabla\boldsymbol{\gamma}, \eta) - \theta\, \eta \right] \tag{2.63}$$

with equivalent expressions for the Coleman relation, driving forces and entropy taking the form

$$\boldsymbol{P} = \frac{\partial A}{\partial \boldsymbol{F}} \tag{2.64}$$

$$\boldsymbol{\tau} = -\frac{\delta A}{\delta \boldsymbol{\gamma}} \tag{2.65}$$

$$\eta = -\frac{\partial A}{\partial T} \tag{2.66}$$

Boundary conditions given by 2.59 read

$$\frac{\partial A}{\partial \nabla \gamma^{\alpha}} \cdot \boldsymbol{N} + \frac{\partial \Pi}{\partial \gamma^{\alpha}} = 0 \qquad \text{on } \partial\Omega \quad , \alpha = 1, \ldots, N \tag{2.67}$$

Evolution laws, also known as *rate equations* or *kinetic relations*, must be supplied to determine the evolution of the internal variables. A common assumption in rate-dependent plasticity theories is that the rate of the internal processes is determined solely by the thermodynamic state. A class of such evolution equations can be written as

$$\dot{\boldsymbol{\gamma}} = f(\boldsymbol{\tau}) \tag{2.68}$$

Rate equations of the class of 2.68 are said to derive from an inelastic potential density if there exists a differentiable function $\psi(\boldsymbol{\tau})$ such that

$$\dot{\boldsymbol{\gamma}} = \frac{\partial \psi(\boldsymbol{\tau})}{\partial \boldsymbol{\tau}} \tag{2.69}$$

A restatement of 2.69 that will prove convenient in the development of variational constitutive updates is presented next. Introduce the inelastic dual potential density, or *disipation potential density* $\psi^*(\dot{\boldsymbol{\gamma}})$ by recourse to the Legendre transform

$$\psi^*(\dot{\boldsymbol{\gamma}}) := \max_{\boldsymbol{\tau}} \boldsymbol{\tau} \cdot \dot{\boldsymbol{\gamma}} - \psi(\boldsymbol{\tau}) \tag{2.70}$$

then, the driving force conjugate to slip can be obtained from the dual potential as

$$\boldsymbol{\tau} = \frac{\partial \psi^*}{\partial \dot{\boldsymbol{\gamma}}} \tag{2.71}$$

due to the properties of the Legendre transform. Substituting the expression for driving forces 2.65 into 2.71 we can express the rate equations as

$$\frac{\delta A}{\delta \boldsymbol{\gamma}} + \frac{\partial \psi^*}{\partial \dot{\boldsymbol{\gamma}}} = 0 \tag{2.72}$$

Up to now, we have considered a general form for the free energy and the dissipation potential. Next, we describe the different mechanisms and processes present in crystal plasticity and their corresponding contribution to the free-energy and dissipation potentials. In metallic materials, the elastic response is ostensibly independent of the internal processes, which justifies an additive decomposition of the bulk free-energy density into elastic energy W^e and plastic energy A^p terms

$$A(\boldsymbol{F}, \boldsymbol{\gamma}, \nabla\boldsymbol{\gamma}) = W^e(\boldsymbol{F}^e) + A^p(\boldsymbol{\gamma}, \nabla\boldsymbol{\gamma}) \tag{2.73}$$

Following Ortiz and Repetto [74], we consider the plastic energy density to be composed of a latent hardening term, which depends on the slip fields and accounts for the interaction between slip systems, and a dislocation self-energy that depends on

the gradient of the slip fields, and introduces a length scale to the plasticity model. Under this assumption, the free-energy density takes the form

$$A(\boldsymbol{F}, \boldsymbol{\gamma}, \nabla\boldsymbol{\gamma}) = W^e(\boldsymbol{F}^e) + W^p(\boldsymbol{\gamma}) + W^{\text{self}}(\nabla\boldsymbol{\gamma}) \tag{2.74}$$

In the following, we treat in detail the particular expressions for the different free-energy components and dissipation potential employed in the constitutive characterization of crystalline materials.

2.2.3.1 Elastic energy

We assume that the elastic response of the crystal follows a Hookean material behavior, and thus express the elastic energy density as

$$W^e(\boldsymbol{F}^e) := \frac{1}{2}\boldsymbol{\varepsilon}^e : \mathbb{C} : \boldsymbol{\varepsilon}^e \tag{2.75}$$

where $\boldsymbol{\varepsilon}^e$ is the *Hencky* or *logarithmic strain* defined by

$$\boldsymbol{\varepsilon}^e := \frac{1}{2}\ln\left(\boldsymbol{F}^{eT}\boldsymbol{F}^e\right) \tag{2.76}$$

By virtue of 2.21, we also have

$$W^e(\boldsymbol{F}^e) = W^e(\boldsymbol{F}\boldsymbol{F}^{p-1}) \tag{2.77}$$

By invoking major and minor symmetries of the elastic moduli tensor, together with cubic material symmetries, we can reduce the number of material constants to three, labeled $\mathbb{C}_{11}$, $\mathbb{C}_{12}$ and $\mathbb{C}_{44}$. The corresponding elastic moduli tensor, in Voight notation, reduces to

$$\mathbb{C} = \begin{bmatrix} \mathbb{C}_{11} & \mathbb{C}_{12} & \mathbb{C}_{12} & 0 & 0 & 0 \\ \mathbb{C}_{12} & \mathbb{C}_{11} & \mathbb{C}_{12} & 0 & 0 & 0 \\ \mathbb{C}_{12} & \mathbb{C}_{12} & \mathbb{C}_{11} & 0 & 0 & 0 \\ 0 & 0 & 0 & \mathbb{C}_{44} & 0 & 0 \\ 0 & 0 & 0 & 0 & \mathbb{C}_{44} & 0 \\ 0 & 0 & 0 & 0 & 0 & \mathbb{C}_{44} \end{bmatrix} \tag{2.78}$$

2.2.3.2 Local plastic stored energy

Ortiz and co-workers [74, 75] proposed a simple model of latent hardening that considers power-law hardening in single slip and off-diagonally dominant isotropic hardening matrix, whose stored energy reads

$$W^p(\boldsymbol{\gamma}) = \sum_{\alpha} \tau_{c0}^{\alpha} \gamma^{\alpha} + \frac{1}{n+1} \tau_0 \gamma_0 \left(\frac{\gamma_{\text{eff}}}{\gamma_0} \right)^{n+1} \tag{2.79}$$

where τ_{c0}^{α} is the initial critical resolved shear stress in the slip system α, τ_0 is a reference resolved shear stress, γ_0 is a reference slip strain, n is a hardening exponent, and

$$\gamma_{\text{eff}} = \sum_{\alpha} \gamma^{\alpha} \tag{2.80}$$

is an effective slip strain.

2.2.3.3 Non-local dislocation self-energy

Dislocation self-energy in the context of continuous dislocation theory was addressed in 2.1.2, and the kinematic relation between dislocation density and continuum measures of deformation was presented in 2.2.1. In particular, the dislocation self-energy of one crystallographic system is obtained by substituting 2.32 into 2.17, which yields

$$E_{\alpha}^{\text{self}}[\gamma^{\alpha}] = \frac{T}{|b|}\int_{\Omega} \|\nabla_{\mathcal{P}^{\alpha}}\gamma^{\alpha}\|_2 \,\mathrm{d}V \tag{2.81}$$

By adding the contribution of all the slip systems, the total dislocation self-energy is

$$\begin{aligned} E^{\text{self}}[\boldsymbol{\gamma}] &= \sum_{\alpha} E_{\alpha}^{\text{self}}[\gamma^{\alpha}] \\ &= \int_{\Omega} \sum_{\alpha} \frac{T}{|b|} \|\nabla_{\mathcal{P}^{\alpha}}\gamma^{\alpha}\|_2 \,\mathrm{d}V \end{aligned} \tag{2.82}$$

and the dislocation self-energy density takes the form

$$W^{\text{self}}(\nabla\boldsymbol{\gamma}) = \sum_{\alpha} \frac{T}{|b|} \|\nabla_{\mathcal{P}^{\alpha}}\gamma^{\alpha}\|_2 \tag{2.83}$$

Anticipating some mathematical difficulties in the solution of systems involving

non-smooth functions like the Euclidean norm in 2.82, we seek an equivalent representation for the dislocation self-energy. We note that the integral in 2.82 corresponds to the *projected total variation*[2] of the function γ^α, which we denote by $V_{\mathcal{P}^\alpha}(\gamma^\alpha, \Omega)$. In particular, one can show[3] that 2.82 admits the following variational characterization,

$$E_\alpha^{\text{self}}[\gamma^\alpha] = \frac{T}{|b|} \sup_{\substack{\phi \in C_c^1(\Omega, \mathbb{R}^n) \\ ||\phi||_{L^\infty(\Omega)} \leq 1}} \int_\Omega \gamma^\alpha \mathcal{P}^\alpha : \nabla \phi \, \mathrm{d}V \tag{2.84}$$

where $\mathcal{P}^\alpha$ was defined in 2.36. In the sequel we assume there exists a solution $\phi^{\alpha,*} \in C_c^1(\Omega, \mathbb{R}^n)$ to the variational problem 2.84,

$$\phi^{\alpha,*} := \underset{\substack{\phi \in C_c^1(\Omega, \mathbb{R}^n) \\ ||\phi||_{L^\infty(\Omega)} \leq 1}}{\arg\sup} \int_\Omega \gamma^\alpha \mathcal{P}^\alpha : \nabla \phi \, \mathrm{d}V \tag{2.85}$$

which we call the *vector potential*. It follows from 2.84 that the total dislocation self-energy of a crystallographic system can be obtained in terms of γ^α only, at the expense of incorporating additional fields - the vector potentials - into the problem.

We conclude this section by noting the connection of the vector potentials with physical quantities of interest. Writing the dislocation self-energy of one slip system in terms of the solution $\phi^{\alpha,*}$, it follows that

$$E_\alpha^{\text{self}}[\gamma^\alpha] = \frac{T}{|b|} \int_\Omega \gamma^\alpha \mathcal{P}^\alpha : \nabla \phi^{\alpha,*} \, \mathrm{d}V \tag{2.86}$$

[2]For the definition of total projected variation, see Appendix A
[3]See Appendix A

Thus, the equivalent dislocation self-energy density reads

$$W_{\alpha}^{\text{self}}(\gamma^{\alpha}) = \frac{T}{|b|}\gamma^{\alpha}\mathcal{P}^{\alpha} : \nabla\phi^{\alpha,*} \tag{2.87}$$

Furthermore, by comparing 2.86 to 2.17, we can express the GND density as

$$\rho_{GND}^{\alpha} := \|\mathsf{A}^{\alpha}\|_{F} = \gamma^{\alpha}\mathcal{P}^{\alpha} : \nabla\phi^{\alpha,*} \tag{2.88}$$

2.2.3.4 Step energy

The disruption of intermolecular bonds that occurs when a step is created on the surface of a solid is quantified by the step energy of a material. Largely neglected in engineering macroscopic material models, surface effects in materials at small scales can markedly influence the mechanical response of a solid. Under the assumption of an isotropic and uniform step energy Γ, the contribution of newly-created step surfaces to the free Helmholtz energy is proportional to the step surface area ΔS,

$$\mathcal{F}^{\text{surf}} := \Gamma \cdot \Delta S \tag{2.89}$$

When a dislocation escapes from the crystal body, it leaves behind a slip step, and therefore increases the step surface of the crystal by an area proportional to the dislocation's Burgers-vector magnitude. Therefore, the flux of dislocations escaping a crystal contribute to the Helmholtz free energy by creating new step surfaces.

Consider a single slip system α in which dislocations escape the crystal through

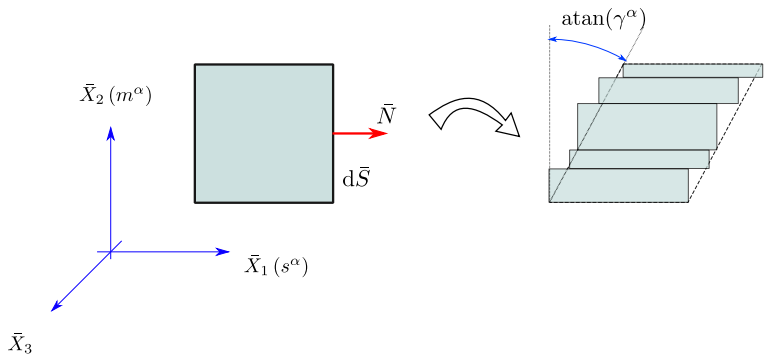

Figure 2.3: Surface formation in crystals.

a differential surface element dS, leaving behind steps, as shown in Figure 2.3. We assume the surface normal to have the same direction as the Burgers vector associated with the slip system. Then, the step area can be conveniently expressed in terms of the slip strain by

$$\mathrm{d}\,\Delta\bar{S} = \gamma^\alpha \mathrm{d}\bar{S} \tag{2.90}$$

If the surface normal $\bar{\boldsymbol{N}}$ does not coincide with the Burgers vector direction $\boldsymbol{s}^\alpha$, the differential surface area d$\bar{S}$ can be found by projecting the crystal surface normal $\boldsymbol{N}$

$$\mathrm{d}\bar{S} = |\bar{\boldsymbol{N}} \cdot (\boldsymbol{N}\mathrm{d}S)| = |\boldsymbol{s}^\alpha \cdot \boldsymbol{N}|\mathrm{d}S \tag{2.91}$$

Thus, integrating over the crystal surface $\partial\Omega$, the step free energy is

$$\Gamma \int_{\partial\Omega} \mathrm{d}\,\Delta\bar{S} = \int_{\partial\Omega} \Gamma\gamma^\alpha |\boldsymbol{s}^\alpha \cdot \boldsymbol{N}|\mathrm{d}S \tag{2.92}$$

Finally, adding the surface effects due to all slip systems we obtain the total step

energy

$$\mathcal{F}^{\text{surf}} = \int_{\partial\Omega} \sum_{\alpha} \Gamma\gamma^{\alpha} |\boldsymbol{s}^{\alpha} \cdot \boldsymbol{N}| \mathrm{d}S \tag{2.93}$$

and the step energy per unit undeformed area reads

$$\Pi(\boldsymbol{\gamma}) = \sum_{\alpha} \Gamma\gamma^{\alpha} |\boldsymbol{s}^{\alpha} \cdot \boldsymbol{N}| \tag{2.94}$$

2.2.3.5 Dissipation potential

In addition to the Helmholtz free energy, a material model needs a dissipation potential to fully describe the irreversible behavior of solids through rate equations. In contrast to the free energy, whose mathematical description can be physically motivated, dissipation potentials prove convenient in the description of evolution laws governing non-equilibrium dissipative processes, and have in general a phenomenological origin. For the case of rate-sensitive metallic crystals, simple phenomenological descriptions of the isothermal rate dependence based on power-law relations have been successfully employed in simulations [76, 17]. In this work, we will consider kinetic relations of the form

$$\dot{\gamma}^{\alpha} = \dot{\gamma}_0 \left(\frac{\max\{0, \tau^{\alpha}\}}{\tau_0} \right)^{\frac{1}{m}} \qquad \alpha = 1, \ldots, N \tag{2.95}$$

where m is the rate-sensitivity exponent, and $\dot{\gamma}_0$, τ_0 are reference strain rate and flow stress, respectively. As noted by Ortiz and Stainier [75], the dissipation potential

density corresponding to 2.95 is

$$\psi^*(\dot{\boldsymbol{\gamma}}) = \begin{cases} \displaystyle\sum_{\alpha=1}^{N} \frac{\tau_0\,\dot{\gamma}_0}{m+1}\left(\frac{\dot{\gamma}^\alpha}{\dot{\gamma}_0}\right)^{m+1} & \text{if } \dot{\gamma}^\alpha \geq 0 \\ \infty & \text{otherwise} \end{cases} \tag{2.96}$$

2.2.4 Equilibrium and kinetics in non-local crystal plasticity

The equilibrium and rate equations governing the non-local crystal plasticity problem can be summarized in the following initial boundary value problem (IBVP),

$$\begin{aligned} \nabla \cdot \frac{\partial A}{\partial \boldsymbol{F}} + \rho_0 \boldsymbol{B} = 0 \qquad & \text{in } \Omega \\ \boldsymbol{\varphi} = \bar{\boldsymbol{\varphi}} \qquad & \text{on } \partial\Omega_1 \\ \frac{\partial A}{\partial \boldsymbol{F}} \boldsymbol{N} = \bar{\boldsymbol{T}} \qquad & \text{on } \partial\Omega_2 \\ \boldsymbol{\varphi}(\boldsymbol{X}, t_1) = \boldsymbol{\varphi}_0(\boldsymbol{X}) \qquad & \text{in } \Omega \\ \frac{\delta A}{\delta \boldsymbol{\gamma}} + \frac{\partial \psi^*}{\partial \dot{\boldsymbol{\gamma}}} = 0 \qquad & \text{in } \Omega \\ \frac{\partial A}{\partial \nabla \boldsymbol{\gamma}} \cdot \boldsymbol{N} + \frac{\partial \Pi}{\partial \boldsymbol{\gamma}} = 0 \qquad & \text{on } \partial\Omega \\ \boldsymbol{\gamma}(\boldsymbol{X}, t_1) = \boldsymbol{\gamma}_0(\boldsymbol{X}) \qquad & \text{in } \Omega \end{aligned} \tag{2.97}$$

In particular, substituting the expressions for the free energy and step energy density, we obtain

$$
\begin{aligned}
\nabla \cdot \frac{\partial W^e}{\partial \boldsymbol{F}} + \rho_0 \boldsymbol{B} = 0 \qquad & \text{in } \Omega \\
\boldsymbol{\varphi} = \bar{\boldsymbol{\varphi}} \qquad & \text{on } \partial\Omega_1 \\
\boldsymbol{P}\boldsymbol{N} = \bar{\boldsymbol{T}} \qquad & \text{on } \partial\Omega_2 \\
\boldsymbol{\varphi}(\boldsymbol{X}, t_1) = \boldsymbol{\varphi}_0(\boldsymbol{X}) \qquad & \text{in } \Omega \\
\frac{\partial W^e}{\partial \gamma^\alpha} + \frac{\partial W^p}{\partial \gamma^\alpha} - \nabla \cdot \left(\frac{T}{|b|} \frac{\nabla_{\mathcal{P}^\alpha} \gamma^\alpha}{\|\nabla_{\mathcal{P}^\alpha} \gamma^\alpha\|_2}\right) + \frac{\partial \psi^*}{\partial \dot{\gamma}^\alpha} = 0 \qquad & \text{in } \Omega, \quad \alpha = 1, \ldots, N \\
\frac{T}{|b|} \frac{\nabla_{\mathcal{P}^\alpha} \gamma^\alpha}{\|\nabla_{\mathcal{P}^\alpha} \gamma^\alpha\|_2} \cdot \boldsymbol{N} + \Gamma |\boldsymbol{s}^\alpha \cdot \boldsymbol{N}| = 0 \qquad & \text{on } \partial\Omega, \quad \alpha = 1, \ldots, N \\
\boldsymbol{\gamma}(\boldsymbol{X}, t_1) = \boldsymbol{\gamma}_0(\boldsymbol{X}) \qquad & \text{in } \Omega
\end{aligned}
\tag{2.98}
$$

We note that the IBVP expressed in 2.98 does not, in general, allow for an analytical solution. Moreover, the rate equations and boundary conditions on the slip fields become singular whenever $\nabla_{\mathcal{P}^\alpha} \gamma^\alpha = 0$, which poses an additional challenge to the solution of the non-local crystal plasticity problem.

Chapter 3

Numerical implementation

3.1 Time integration

The numerical time integration of constitutive material models has been a subject of intense research over the last fifty years. A general review of inelastic constitutive updates can be found in [85]. In this work, we follow the variational constitutive updates developed by Ortiz and co-workers [74, 75, 79, 93]. This rather general framework is intended for elasto-viscoplastic solids, and it is particularly well suited for material models conforming to the internal-variable thermodynamic formalism, under which our non-local plasticity model has been developed.

As noted in section 2.2.4, the equivalent formulation of the non-local crystal plasticity model incorporates additional fields, the vector potentials, to the problem, thus increasing its dimensionality. Consequently, one should expect a numerical implementation with a higher number of unknowns that need to be solved for, which in turn implies a more computationally demanding problem. In order to make the numerical problem tractable, it will prove convenient to adopt a staggered-procedure

approach [26], where we consider two independent problems: the mechanical problem, described by the deformation mapping that determines the current configuration, and the vector-potential problem. Thus, during a mechanical step, the vector potentials are held constant, and the deformation mapping is updated. The evolution of the vector potential is then solved for in a similar fashion, by holding constant the current configuration while the vector-potentials nodal values are solved for. It follows that, under this approach, our formulation is local in the internal variables $\boldsymbol{\gamma}$, and therefore amenable to variational constitutive updates.

3.1.1 Variational constitutive updates

The integration of the free-energy density 2.74 over the crystal domain plus the step energy 2.93 yields the total free energy of the crystal, which takes the form

$$\mathcal{F}[\boldsymbol{\varphi},\boldsymbol{\gamma}] = \int_\Omega \left\{ W^e(\boldsymbol{F}\boldsymbol{F}^{p-1}) + W^p(\boldsymbol{\gamma}) + \sum_\alpha \frac{T}{|b|}\gamma^\alpha \mathcal{P}^\alpha : \nabla\phi^{\alpha,*} \right\} \mathrm{d}V + \int_{\partial\Omega} \sum_\alpha \Gamma\gamma^\alpha |\boldsymbol{s}^\alpha \cdot \boldsymbol{N}| \mathrm{d}S \tag{3.1}$$

where we have considered the alternative representation for the dislocation self-energy 2.87. We consider distributing the step energy across the thickness of a boundary layer, whose domain we define by Ω_ϵ and thickness we denote by ϵ. Thus, we arrive to an approximation of the free energy of the form

$$\mathcal{F}^\epsilon[\boldsymbol{\varphi},\boldsymbol{\gamma}] = \int_\Omega A^\epsilon(\boldsymbol{F}\boldsymbol{F}^{p-1}, \boldsymbol{\gamma}, \nabla\boldsymbol{\phi}^*)\, \mathrm{d}V \tag{3.2}$$

where the free-energy density is defined by

$$A^{\epsilon}(\boldsymbol{F}\boldsymbol{F}^{p-1},\boldsymbol{\gamma},\nabla\boldsymbol{\phi}^{*}) = W^{e}(\boldsymbol{F}\boldsymbol{F}^{p-1})+W^{p}(\boldsymbol{\gamma})+\sum_{\alpha}\frac{T}{|b|}\gamma^{\alpha}\mathcal{P}^{\alpha}:\nabla\phi^{\alpha,*}+\chi_{\epsilon}\sum_{\alpha}\frac{\Gamma}{\epsilon}\gamma^{\alpha}|\boldsymbol{s}^{\alpha}\cdot\boldsymbol{N}| \tag{3.3}$$

and

$$\chi_{\epsilon}(\boldsymbol{X}) := \begin{cases} 1 & \text{if } \boldsymbol{X}\in\Omega_{\epsilon} \\ \\ 0 & \text{otherwise} \end{cases} \tag{3.4}$$

is the characteristic function for the boundary layer. The consideration of ϵ-neighborhoods for approximating surface terms in energy functionals, and its convergence in brittle fracture problems has been addressed by Schmidt, Fraternali and Ortiz [82].

It follows that, under the consideration of a staggered procedure where $\boldsymbol{\phi}^{*}$ is kept fixed during a time step, the free-energy density 3.3 is local in the slip fields $\boldsymbol{\gamma}$, thus conforming to the type of free-energy densities upon which the variational constitutive updates are formulated [75, 79]. The idea is then to reduce the evolution problem to a series of equivalent static problems by recourse to time discretization. Consider a generic time interval $[t_n, t_{n+1}]$ with time step $\Delta t = t_{n+1} - t_n$, where all the fields are assumed known for $t = t_n$, and fix the vector potential fields to the previously known values, i.e., $\boldsymbol{\phi}^{*}_{n}$. We define the *incremental energy density* as

$$W(\boldsymbol{F}_{n+1};\boldsymbol{F}_{n},\boldsymbol{\gamma}_{n},\nabla\boldsymbol{\phi}^{*}_{n}) = \min_{\Delta\boldsymbol{\gamma}\succeq 0}\left\{A^{\epsilon}(\boldsymbol{F}_{n+1}\boldsymbol{F}^{p-1}_{n+1},\boldsymbol{\gamma}_{n+1},\nabla\boldsymbol{\phi}^{*}_{n}) - A^{\epsilon}_{n} + \Delta t\,\psi^{*}\left(\frac{\Delta\boldsymbol{\gamma}}{\Delta t}\right)\right\} \tag{3.5}$$

where

$$A_n^\epsilon = A^\epsilon(\boldsymbol{F}_n \boldsymbol{F}_n^{p-1}, \boldsymbol{\gamma}_n, \nabla \boldsymbol{\phi}_n^*) \tag{3.6}$$

and $\Delta\boldsymbol{\gamma} = \boldsymbol{\gamma}_{n+1} - \boldsymbol{\gamma}_n$. Minimization with respect to $\boldsymbol{\gamma}_{n+1}$ in equation 3.5 implies

$$\boldsymbol{\tau}_{n+1} = \frac{\partial \psi^*(\frac{\Delta\boldsymbol{\gamma}}{\Delta t})}{\partial \boldsymbol{\gamma}_{n+1}} \tag{3.7}$$

which is the time-discretized version of the rate equations 2.95. Moreover, the stress update is

$$\boldsymbol{P}_{n+1}(\boldsymbol{F}) = \frac{\partial W(\boldsymbol{F}; \boldsymbol{F}_n, \boldsymbol{\gamma}_n, \nabla \boldsymbol{\phi}_n^*)}{\partial \boldsymbol{F}_{n+1}} \tag{3.8}$$

i.e., the stress update possesses a potential structure. The consistency of the variational constitutive updates has been established in [75, 79].

3.1.2 Flow-rule update

In writing 3.5 we have assumed $\boldsymbol{F}_{n+1}^p$ is known from the integration of flow rule 2.31. The numerical integration of flow rules in finite-deformation plasticity has been approached in several different ways in the literature. In particular, the use of the exponential mapping in the integration of finite-deformation flow rules, and first order approximations thereof, has been considered by [92, 24, 16, 61]. One appealing aspect of the exponential mapping is that it yields an updated plastic deformation gradient that automatically satisfies plastic incompressibility, a condition that follows from the tracelessness of plastic flow rules. However, exponential mappings may be

costly to compute, especially their first and second tangents [73], which are usually needed in the solution of non-linear equations using iterative methods like Newton-Raphson. In the following, we propose an incremental update inspired on the theory of differentiable manifolds [60].

As discussed in 2.2.1, the plastic deformation gradient $\boldsymbol{F}^p$ conforms to the incompressibility condition set by 2.22. From a set-theory standpoint, $\boldsymbol{F}^p$ is an element of the special linear group $SL(3) = \left\{\boldsymbol{A} \in \mathbb{R}^{3\times3} | \det(\boldsymbol{A}) = 1\right\}$, and it can be further shown (c.f. [60]) that $SL(3)$ is a differentiable manifold[1], with tangent space being defined by $\mathfrak{sl}(3) = \left\{\boldsymbol{a} \in \mathbb{R}^{3\times3} | \text{trace}(\boldsymbol{a}) = 0\right\}$, the set of traceless matrices. In particular, the plastic velocity gradient defined in 2.25 is an element of the tangent space just defined. Figure 3.1 shows a geometric interpretation of these concepts.

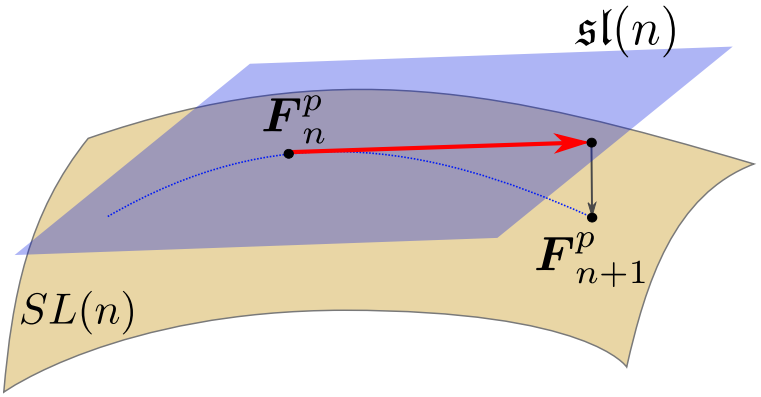

Figure 3.1: Special-linear update.

By *updates* we understand a mapping that takes a point in the tangent space $\mathfrak{sl}(3)$ and projects it back to the manifold $SL(3)$, subject to certain consistency conditions.

[1] and consequently a Lie group

A classical example of updates in Riemannian manifolds and Lie groups is the exponential mapping. For a rigorous definition of updates in differential manifolds, see [71]. Let $A \in SL(3)$ and $a \in \mathfrak{sl}(3)$. A simple update[2] for the special linear manifold is

$$\mathrm{upd}(\boldsymbol{a}) = \frac{\boldsymbol{A} + \boldsymbol{a}}{\det^{\frac{1}{3}}(\boldsymbol{A} + \boldsymbol{a})} \tag{3.9}$$

In the particular case of single-crystal plasticity and assuming a backward Euler approximation for the slip rate, we set $\boldsymbol{A} = \boldsymbol{F}_n^p$ and $\boldsymbol{a} = \sum_\alpha \Delta\gamma^\alpha \boldsymbol{s}^\alpha \otimes \boldsymbol{m}^\alpha$. Thus, the *special-linear update* inspired on 3.9 reads

$$\boldsymbol{F}_{n+1}^p(\Delta\boldsymbol{\gamma}; \boldsymbol{F}_n^p) = \frac{\boldsymbol{I} + \sum_\alpha \Delta\gamma^\alpha \boldsymbol{s}^\alpha \otimes \boldsymbol{m}^\alpha}{\det^{\frac{1}{3}}\left(\boldsymbol{I} + \sum_\alpha \Delta\gamma^\alpha \boldsymbol{s}^\alpha \otimes \boldsymbol{m}^\alpha\right)} \boldsymbol{F}_n^p \tag{3.10}$$

and Figure 3.1 provides a geometric interpretation of the update. Appendix C contains the expressions for the first and second tangents of the update 3.9.

The proposed special-linear update for the crystallographic flow rule has been integrated into a general finite-kinematics version of a local crystal-plasticity model based on the variational constitutive updates framework. Figure 3.2 shows the comparison of the special-linear and exponential update. The difference in the numerical results between the two updates is only noticeable at moderate strains ($> 10\%$). In order to show the applicability of the proposed flow-rule update, we have performed a parameter fitting using the experimental results for copper single crystals by Franciosi and Zaoui [31], using the dislocation-based hardening model developed by Cuitino and

[2]Since it corresponds to the submersion of an element in the tangent space, see [71]

Ortiz [16] in the variational form of Ortiz and Stainier [75]. The experimental data and simulated stress-strain curves for two highly-symmetrical orientations ([001] and [111]) are shown in Figure 3.3. These loading orientations lead to polyslip condition [49], activating eight and six slip systems, respectively. The numerical implementation correctly captures the set of active slip systems, as observed in the slip strain curves in Figure 3.4. The material parameters used in the numerical simulations for copper single crystals are listed in Table 3.1.

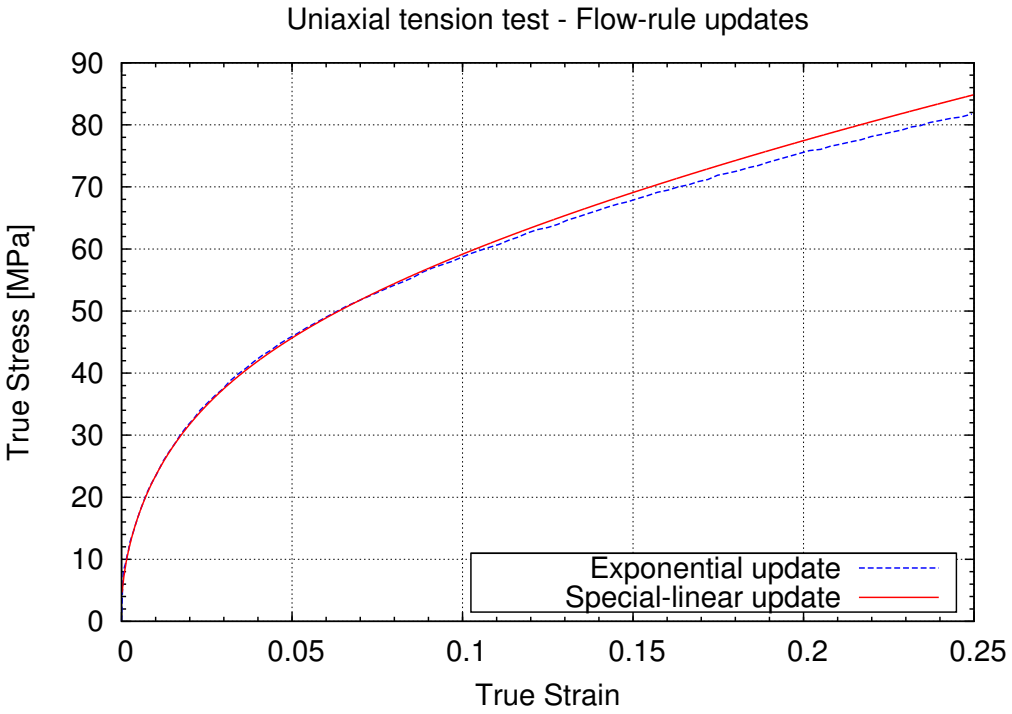

Figure 3.2: Comparison of flow-rule updates. Exponential case is taken from [75].

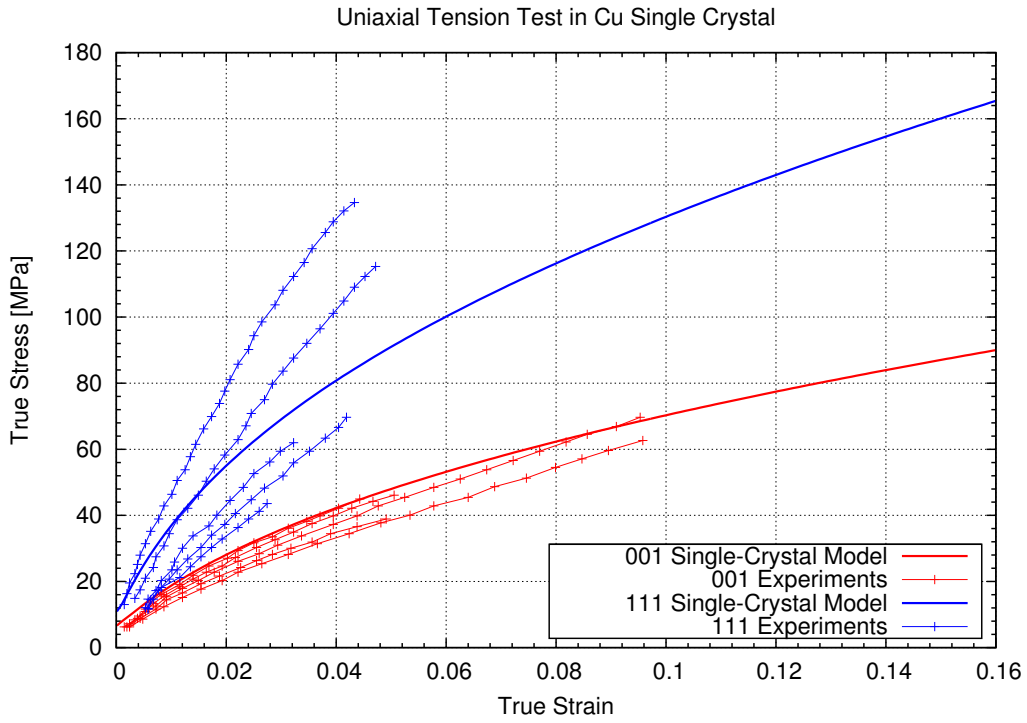

Figure 3.3: Dislocation-based model fitting. Experimental data is taken from [31].

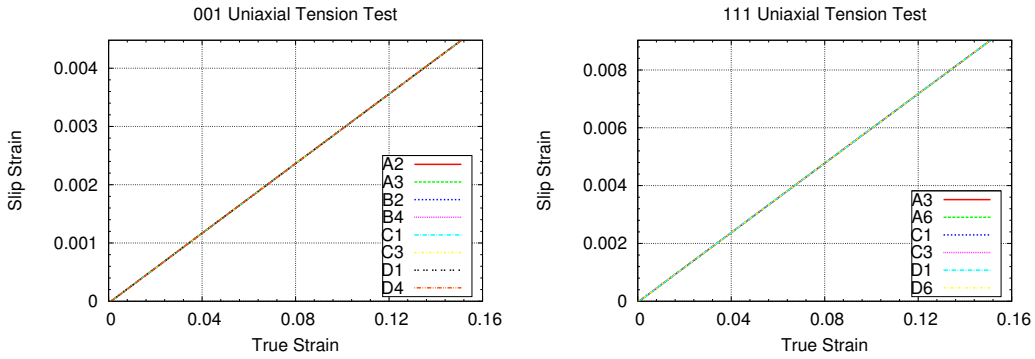

(a) 001 Loading direction (b) 111 Loading direction

Figure 3.4: Active slip systems and slip strain.

3.2 Spatial integration using the finite element method

3.2.1 The mechanical problem

As mentioned in section 3.1.1, the solution to the rate problem in crystal plasticity can be reduced to a sequence of equivalent static problems by means of constitutive

$\mathbb{C}_{11}$	168.4×10^3 MPa
$\mathbb{C}_{12}$	121.4×10^3 MPa
$\mathbb{C}_{44}$	75.4×10^3 MPa
γ_0	1.0
m	100
τ_0	2.0 MPa
ρ_0	$1.0 \times 10^{10}\,\mathrm{m}^{-2}$
ρ_{sat}	$1.0 \times 10^{13}\,\mathrm{m}^{-2}$
γ_{sat}	0.5%
a_0	8.0×10^{-4}
a_1	$5.7\,a_0$
a_2	$10.2\,a_0$
a_3	$16.6\,a_0$
α	0.3
b	2.56×10^{-10}
μ	75.4×10^3 MPa

Table 3.1: Model parameters for copper single crystal.

variational updates. By approximating the first Piola-Kirchhoff tensor in the linear momentum balance equation 2.39 by the stress update 3.8, the equivalent static problem for a generic time step t_{n+1} takes the form

$$\begin{aligned} \nabla \cdot \boldsymbol{P}_{n+1}(\nabla \boldsymbol{\varphi}_{n+1}) + \rho_0\, \boldsymbol{B}_{n+1} = 0 \qquad & \text{in } \Omega \\ \boldsymbol{\varphi}_{n+1} = \bar{\boldsymbol{\varphi}}_{n+1} \qquad & \text{on } \partial\Omega_1 \\ \boldsymbol{P}_{n+1}(\nabla \boldsymbol{\varphi}_{n+1})\boldsymbol{N} = \bar{\boldsymbol{T}}_{n+1} \qquad & \text{on } \partial\Omega_2 \end{aligned} \tag{3.11}$$

where $\boldsymbol{\varphi}_{n+1} : \Omega \to \mathbb{R}^3$ is the time-discretized displacement field we need to solve for, and

$$\boldsymbol{B}_{n+1} = \boldsymbol{B}(\boldsymbol{X}, t_{n+1}) \quad , \quad \bar{\boldsymbol{\varphi}}_{n+1} = \bar{\boldsymbol{\varphi}}(\boldsymbol{X}, t_{n+1}) \quad , \quad \bar{\boldsymbol{T}}_{n+1} = \bar{\boldsymbol{T}}(\boldsymbol{X}, t_{n+1})$$

are prescribed functions. Due to the potential structure of the stress update 3.8, the boundary value problem 3.11 resembles an elastostatics problem, and therefore admits the following variational formulation [59, 72],

$$\Phi[\boldsymbol{\varphi}_{n+1}] = \inf_{\boldsymbol{\eta} \in \mathcal{V}} \Phi[\boldsymbol{\eta}] \tag{3.12}$$

where $\Phi[\cdot]$ is the potential energy defined by

$$\Phi[\boldsymbol{\varphi}_{n+1}] = \int_\Omega W(\nabla \boldsymbol{\varphi}_{n+1}; \boldsymbol{F}_n, \boldsymbol{\gamma}_n, \nabla \boldsymbol{\phi}_n^*) \, \mathrm{d}V - \int_\Omega \rho_0 \boldsymbol{B}_{n+1} \cdot \boldsymbol{\varphi}_{n+1} - \int_{\partial\Omega_2} \boldsymbol{T}_{n+1} \cdot \boldsymbol{\varphi}_{n+1} \, \mathrm{d}S \tag{3.13}$$

and the space of solutions $\mathcal{V} \in W^{1,\infty}(\Omega, \mathbb{R}^3)$ satisfies the essential boundary conditions 2.48.

Based on the variational restatement 3.12 of the equivalent static problem, we formulate the associated finite-element problem. Following the Rayleigh-Ritz method, we consider a sequence of approximating finite-dimensional subspaces $\mathcal{V}^h \subset \mathcal{V}$. In particular, we consider a finite-element discretization of the domain Ω, and *trial*

functions $\boldsymbol{\eta}^h \in \mathcal{V}^h$ of the form

$$\boldsymbol{\eta}^h(\boldsymbol{X}) = \sum_{a \in \mathcal{A}} N_a(\boldsymbol{X}) \boldsymbol{\eta}_a \tag{3.14}$$

where $\mathcal{A}$ is the nodal set for the discretization of Ω, $\boldsymbol{\eta}_a \in \mathbb{R}^3, a \in \mathcal{A}$ are the nodal value of the trial function, and $N_a : \Omega \to \mathbb{R}, a \in \mathcal{A}$ are the *basis* or *shape functions* satisfying the Kronecker-delta property

$$N_a(\boldsymbol{X}_b) = \begin{cases} 1 & \text{if } a = b \\ 0 & \text{otherwise} \end{cases} \tag{3.15}$$

Then, the Ritz approximation is the function $\boldsymbol{\varphi}^h_{n+1} \in \mathcal{V}$ that minimizes the potential energy, i.e.,

$$\boldsymbol{\varphi}^h_{n+1} := \underset{\boldsymbol{\eta}^h \in \mathcal{V}^h}{\arg\inf}\ \Phi[\boldsymbol{\eta}^h] \tag{3.16}$$

3.2.2 Incompressibility and mean-dilatation elements

Standard finite-element formulations based on linear shape functions suffer from volumetric locking in problems involving near-incompressibility. A customary assumption in metal plasticity is the isochoric evolution of the inelastic deformations, as stated in 2.22. Several approaches have been proposed in the literature to deal with such internal constraints and alleviate locking, including local bubble enrichment for dis-

placements [15], mixed formulations [23] and mean-dilatation methods [63] and their generalization using assumed-strain methods [45], among others. (For a review, see [46, 23, 40].)

In this work, we consider a mean-dilatation approach for finite kinematics inspired in its linear counterpart (c.f. [63]). Following [40], we take the volumetric and deviatoric components of the deformation gradient to be

$$\boldsymbol{F}^{\text{vol}} = J^{\frac{1}{3}}\boldsymbol{I} \tag{3.17}$$

$$\boldsymbol{F}^{\text{dev}} = J^{-\frac{1}{3}}\boldsymbol{F} \tag{3.18}$$

which defines the following multiplicative decomposition of the deformation gradient

$$\boldsymbol{F} = \boldsymbol{F}^{\text{dev}}\boldsymbol{F}^{\text{vol}} \tag{3.19}$$

It can be shown that a linearization of 3.17 and 3.18 about the undeformed configuration (i.e., $\boldsymbol{F} = \boldsymbol{I}$) in the direction of the displacement field $\boldsymbol{u}$ yields

$$< D\,\boldsymbol{F}^{\text{vol}}, \boldsymbol{u} > = \frac{1}{3}(\operatorname{div}\boldsymbol{u})\boldsymbol{I} \tag{3.20}$$

$$< D\,\boldsymbol{F}^{\text{dev}}, \boldsymbol{u} > = \nabla\boldsymbol{u} - \frac{1}{3}(\operatorname{div}\boldsymbol{u})\boldsymbol{I} \tag{3.21}$$

which is the standard decomposition, in the linearized-kinematics setting, of the displacement gradient into volumetric and deviatoric components.

The concept of mean dilatation can be extended to the context of finite kinematics as follows. The logarithmic volumetric strain is defined as

$$\theta = \log(J) \tag{3.22}$$

Let Ω_e be the domain of the finite element under consideration. Then, the mean dilatation can be obtained by averaging 3.22 over the element volume

$$\bar{\theta} = \log(\bar{J}) = \frac{1}{|\Omega_e|} \int_{\Omega_e} \log(J(\boldsymbol{X}))\, \mathrm{d}V \tag{3.23}$$

Then, based on the decomposition 3.19, we define the mean-dilatation deformation gradient as

$$\bar{\boldsymbol{F}} = J^{-\frac{1}{3}} \boldsymbol{F}\, \bar{J}^{\frac{1}{3}} \boldsymbol{I} = \bar{J}^{\frac{1}{3}} J^{-\frac{1}{3}} \boldsymbol{F} \tag{3.24}$$

and use this version of the deformation gradient in the evaluation of the material energy density and its derivatives, as needed in the calculation of the finite element energy, nodal forces and tangent stiffness. In addition to the mean-dilatation approach, we consider enriching the linear interpolation basis by adding bubble nodes in the faces of tetrahedral elements, as depicted in Figure 3.5.

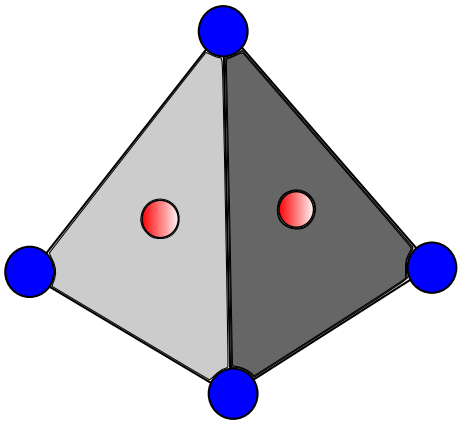

Figure 3.5: Tetrahedral element with bubbles in its faces.

3.2.3 The vector-potential problem

The local form of the dislocation self-energy for the slip system α given in 2.84 hinges on the solution of the following variational problem,

$$\sup_{\substack{\phi^\alpha \in C_c^1(\Omega,\mathbb{R}^n) \\ ||\phi^\alpha||_{L^\infty(\Omega)} \leq 1}} \int_\Omega \gamma^\alpha \mathcal{P}^\alpha : \nabla \phi^\alpha \, \mathrm{d}V \tag{3.25}$$

We note that 3.25 depends only on the slip field of the α slip system, and therefore is independent of other slip systems. Therefore, we will have as many vector-potential independent problems to solve as active slip systems. The solutions to these problems are further needed in the computation of the total dislocation self-energy, as defined in 2.82.

A finite-element formulation for the vector-potential problem can be obtained in a similar fashion to the mechanical problem. We assume the same discretization of the domain used in the mechanical problem, and consider trial functions similar to

3.14, which in this case read

$$\boldsymbol{\phi}^{\alpha,h}(\boldsymbol{X}) = \sum_{a\in\mathcal{A}} N_a(\boldsymbol{X})\boldsymbol{\phi}_a^\alpha \tag{3.26}$$

where $\boldsymbol{\phi}_a^\alpha \in \mathbb{R}^3$, $a \in \mathcal{A}$ are the vector-potential nodal values. The trial function gradient reads

$$\nabla\boldsymbol{\phi}^{\alpha,h}(\boldsymbol{X}) = \sum_{a\in\mathcal{A}} \boldsymbol{\phi}_a^\alpha \otimes \nabla N_a(\boldsymbol{X}) \tag{3.27}$$

Substituting 3.27 into 3.25 we arrive at the following optimization problem,

$$\begin{aligned} &\text{Maximize} && \sum_{a\in\mathcal{A}} \boldsymbol{f}^{\alpha,a}\cdot\boldsymbol{\phi}_a^\alpha \\ &\text{subject to} && \|\boldsymbol{\phi}_a^\alpha\|_2 \leq 1 \quad , a\in\mathcal{A} \end{aligned} \tag{3.28}$$

where

$$\boldsymbol{f}^{\alpha,a} = \int_\Omega \gamma^\alpha \mathcal{P}^\alpha : \nabla N_a(\boldsymbol{X})\,\mathrm{d}V \tag{3.29}$$

A few remarks on 3.28 are in order. We first note that solving 3.28 is equivalent to solving a set of independent problems of the form

$$\left.\begin{aligned} &\text{Maximize} && \boldsymbol{f}^{\alpha,a}\cdot\boldsymbol{\phi}_a^\alpha \\ &\text{subject to} && \|\boldsymbol{\phi}_a^\alpha\|_2 \leq 1 \end{aligned}\right\} \quad \forall a\in\mathcal{A} \tag{3.30}$$

due to the independence of constraints in 3.28. The objective function of the equivalent sub-problem in 3.30 is affine on the vector-potential nodal coordinates, and therefore concave. Further, the constraint function is convex since it is an affine

transformation of a norm, and thus 3.30 represents a set of independent convex problems. Moreover, the origin is always a strictly feasible point of 3.30, and consequently Slater's conditions hold. In particular, the Karush-Kuhn-Tucker conditions provide necessary and sufficient conditions for optimality [13], which in this case take the form

$$\begin{gathered} \boldsymbol{f}^{\alpha,a} + \lambda \frac{\phi_a^{\alpha,*}}{\|\boldsymbol{\phi}_a^{\alpha,*}\|_2} = 0 \\ \|\boldsymbol{\phi}_a^{\alpha,*}\|_2 - 1 \leq 0 \\ \lambda \geq 0 \\ \lambda \left(\|\boldsymbol{\phi}_a^{\alpha,*}\|_2 - 1\right) = 0 \end{gathered} \tag{3.31}$$

It follows that a solution to 3.31 and in turn to 3.30 is

$$\phi_a^{\alpha,*} = \begin{cases} \dfrac{\boldsymbol{f}^{\alpha,a}}{\|\boldsymbol{f}^{\alpha,a}\|_2} & \text{if } \boldsymbol{f}^{\alpha,a} \neq 0 \\ 0 & \text{otherwise} \end{cases} \tag{3.32}$$

3.3 Computational aspects

Multiscale material models pose a challenge to numerical simulations, due to the many expensive calculations at the material level they involve. In particular, the determination of the local state at the quadrature point level in finite element (FE) simulations using crystal plasticity material models represents a high portion of the total computation time. Moreover, the computation time grows linearly with the number of elements considered in the problem, leading to a compromise between the accuracy of the material model and the accuracy of the FE discretization. In order

to handle such challenging computational demands, one needs to resort to parallel computing.

The numerical framework described in the foregoing has been implemented in `Eureka`.[3] A very general description of the hierarchy of classes in a FE problem in `Eureka`, which is standard for modern FE codes in general, is shown in Figure 3.6. As already mentioned, the evaluation of multiscale material models at the quadrature points takes the highest share of the computation time in multiscale simulations. Therefore, for problems where the number of finite elements in the model is not too large and domain decomposition is not necessary, a plausible strategy for parallelization consists in the parallel evaluation of the material response at the quadrature points. We therefore identify the *fine-grain task* with one material model evaluation, which is performed by the `Material` class.

There are several advantages to the strategy just described, which in High-Performance Computing (HPC) is known as a Single-Instruction-Multiple-Data (SIMD) model. First, the partition of the problem can be done arbitrarily, that is, one can assign a set of quadrature points to a process regardless of the finite element they belong to. Since the crystal plasticity material model is local, no communications between processes are needed while performing material calculations, and the only information exchange occurs at the initialization of a process, where the material model receives as input the deformation gradient, and when the material response has been computed,

[3] `Eureka` is a `C++` finite element code developed by Michael Ortiz

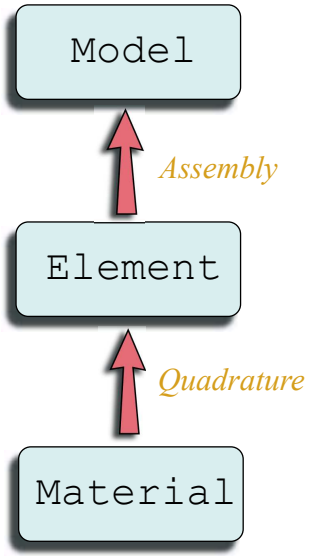

Figure 3.6: Finite element model hierarchy.

and the result needs to be communicated to the `Element` class in the quadrature process. Since there is little communication between fine-grain tasks, the task coarsening is simply done by assigning more quadrature points to a single process.

The parallelization strategy just described has been implemented for shared-memory machines using the POSIX threads library. Table 3.2 summarizes the size of the FE model considered in the evaluation of the performance of the parallel implementation, along with the execution time for one evaluation of the `model` potential energy. A commonly used performance metric in HPC is the *speedup*, which is defined as

$$S_p = \frac{T_1}{T_p} \tag{3.33}$$

where p is the number of threads, T_1 is the execution time of a sequential implementation and T_p is the execution time of the parallel implementation using p threads.

Linear or *ideal speedup* is achieved whenever $S_p = p$. Figure 3.7 shows the speedups obtained for the parallel implementation developed, based on the results shown in Table 3.2. We conclude that the parallel implementation obtains almost ideal speedup, which is indicative of good scalability, a very desirable feature in the development of parallel computer codes.

Elements	DOFs	Execution time (sec)				
		Sequential	2 Threads	4 Threads	8 Threads	16 Threads
576	225	118.880	60.239	30.169	15.300	7.870
1152	441	245.456	121.749	60.749	30.628	16.200
2304	1065	414.287	206.878	103.987	53.457	27.211

Table 3.2: FE mesh information and execution times.

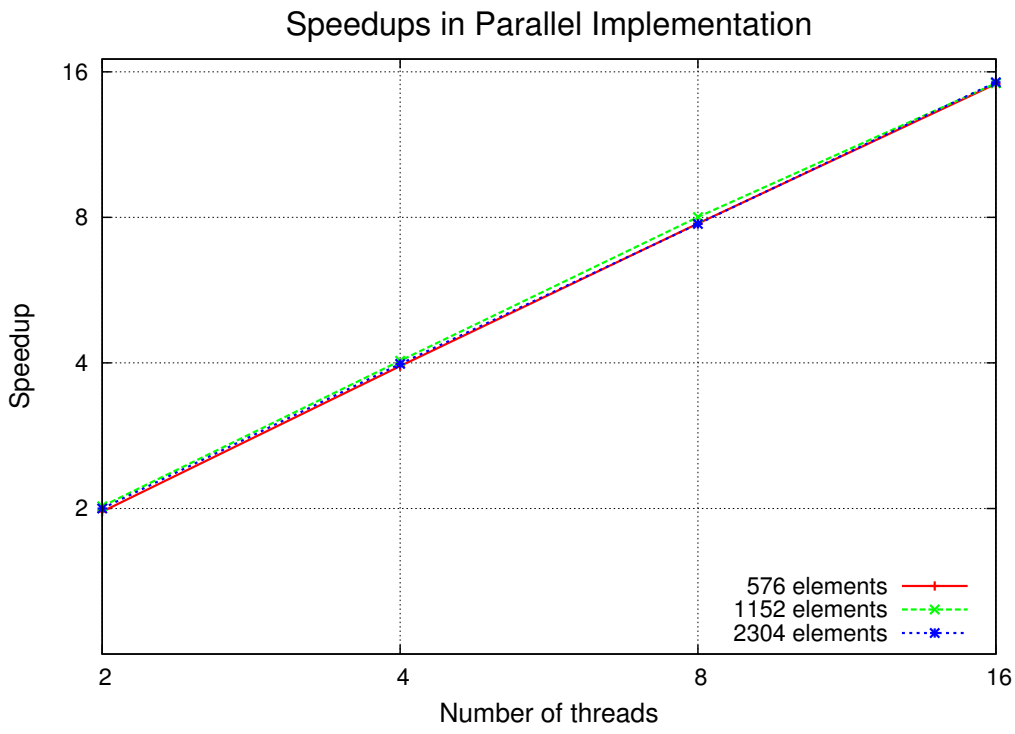

Figure 3.7: Performance metrics - speedups.

Chapter 4

Model validation

4.1 Introduction

Due to their simple geometry, micropillars in compression tests allow for a more direct study of microplasticity. In contrast with torsion experiments on metallic whiskers, where strain gradients are predominant throughout the sample, micropillar compression tests involve low strain gradients, and therefore allow us to study other deformation mechanisms directly related to the physical dimensions of the sample. Figure 4.1 shows a micropillar sample before and after being tested in compression.

The mechanical response of FIB-machined nickel micropillars was systematically studied by Dimiduk and co-workers [21] by means of quasi-static room-temperature axial compression tests. By varying the micropillar diameter over the range of $1 - 40\,\mu$m, they found a strong dependence of the yield stress on the sample diameter for the case of micropillars with diameter below 10 μm, while samples with diameters in the 20-40 μm range would result in yield stresses of the order of nickel bulk sub-millimeter single crystals. The uniaxial stress-strain curves of representative

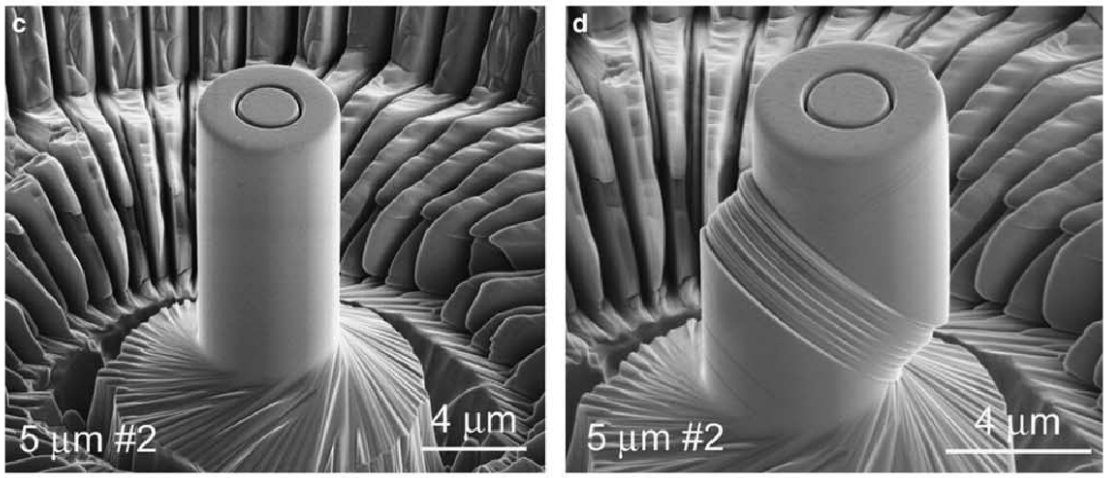

Figure 4.1: Micropillar sample before and after compression test. Taken from [21].

experiments for the different diameters tested are shown in Figure 4.2.

4.2 Numerical simulation of nickel micropillars

Motivated by the work of Dimiduk et al. [21], numerical simulations of nickel single-crystal micropillars have been performed using the model developed in the foregoing. The sample lattice was oriented so that the vertical axis corresponds to the [2 6 9] direction of the crystal, thus predominantly activating the A3 slip system under uni-axial loading. The Schmid factor associated with this loading condition is 0.48. The top and bottom of the pillar were clamped, and the numerical test consisted in a displacement-controlled compression experiment. Pillar diameters of 1, 2.5, 5, 10 and 30 μm were tested, while the height-to-diameter aspect ratio was fixed at 2.5 for all simulations. The nominal axial strain rate was $1 \times 10^{-1}\,\mathrm{s}^{-1}$ for all tests. The mesh

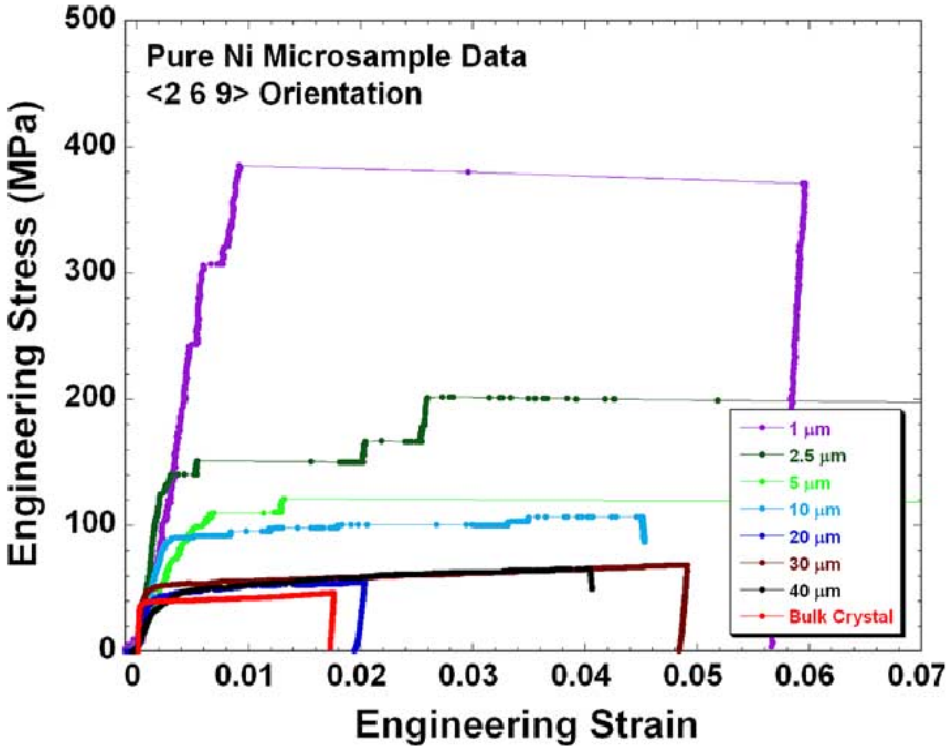

Figure 4.2: Representative stress-strain curves for different sample diameters. Taken from [21].

was refined until the longest edge of the largest tetrahedral element measured less than 0.3 pillar diameters.

The material model parameters used in simulations can be found in Table 4.1, and were selected as follows. The elastic moduli $\mathbb{C}_{11}, \mathbb{C}_{12}, \mathbb{C}_{44}, \mu$ were obtained from the literature [84]. The Burgers-vector magnitude b was assumed to be equal to the lattice parameter for nickel. The critical resolved shear stress τ_{c0}^{α} matches the average value found by Dimiduk and co-workers [21] in macroscopic nickel crystals. In view of the low hardening rates in easy-glide stage observed in experimental results, we have considered the power-law hardening model described in 2.2.3.2, with parabolic

hardening in single slip and a reference resolved shear stress equal to 10% of the critical resolved shear stress, which approximates a rigid-plastic response, as shown in Figure 4.3. The geometrical factor for the dislocation self-energy α was set to 0.1 to also reflect low hardening in easy glide. Values for the step formation energy of FIB-damaged nickel samples were not in the literature, so its value was selected to best match experimental results. The fitting procedure consisted in iterating the value of the step formation energy until a good match was found for the 1 μm-diameter pillar case. Then, the fitted step formation energy value was assumed constant for all other micropillar samples.

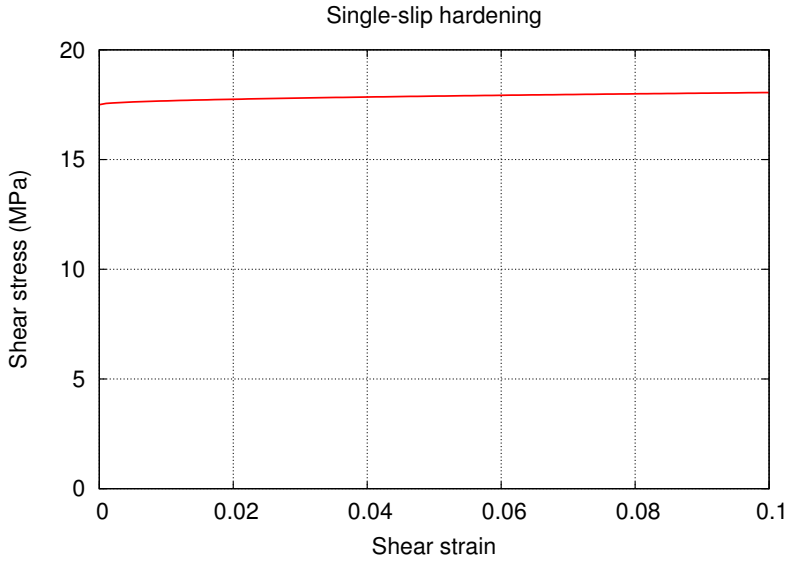

Figure 4.3: Local resolved shear stress for single slip.

Elastic Energy	$\mathbb{C}_{11}$	247.0×10^3 MPa
	$\mathbb{C}_{12}$	147.0×10^3 MPa
	$\mathbb{C}_{44}$	125.0×10^3 MPa
Local Plastic Energy	τ_{c0}^{α}	17.5 MPa
	τ_0	$0.1 \cdot \tau_{c0}^{\alpha} = 1.75$ MPa
	γ_0	1.0
	n	0.5
Dislocation Self-Energy	α	0.1
	μ	79.0×10^3 MPa
	b	3.52×10^{-10} m
Step-formation Energy	Γ	$90.0\,\mathrm{J/m^2}$
Dissipation Potential	$\dot{\gamma}_0$	1.0
	Y_0	17.5 MPa
	m	0.05

Table 4.1: Material model parameters for Ni micropillars.

4.3 Results and discussion

The simulated and experimental stress-strain curves for nickel micropillars with diameters 1, 2.5, 5, 10 and 30 μm are plotted in Figure 4.4. We start the discussion by noting the apparent difference in tangent modulus of the simulated and experimental curves. As noted in [21], one of the difficulties of compression tests in microsamples is to obtain perfect alignment between the surface of the flat indenter used to compress the sample and the micropillar top. The discrepancies between the theoretical and experimental loading tangent moduli can be attributed to misalignment, along with the compliance provided by the bottom substrate supporting the pillar on the overall response, as argued by Greer et al. [36].

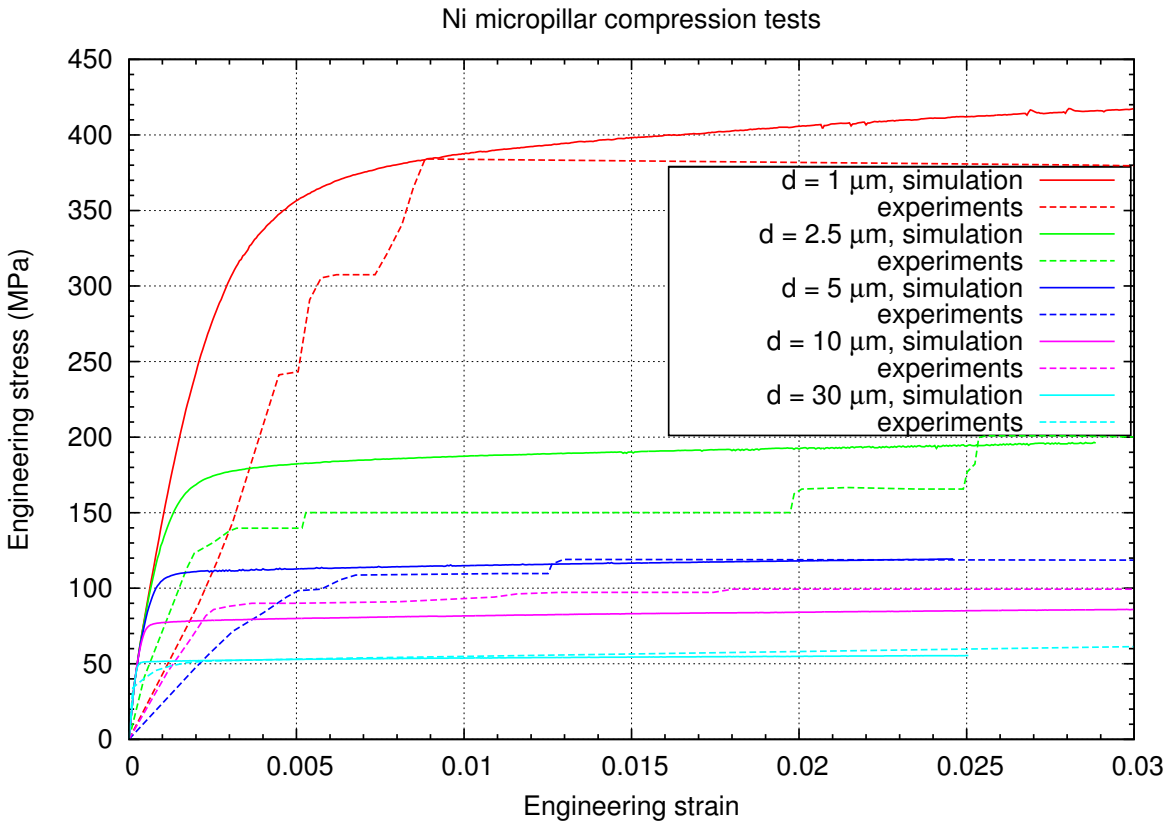

Figure 4.4: Stress-strain curves for simulations and experiments.

Several authors consider different levels of strain for the comparison of flow stresses in micropillar tests. The arbitrariness of the strain level considered for determining the sample strength is mainly due to random strain bursts encountered in the stress-strain curves, particularly for small diameter samples, which do not allow for a characteristic curve to be identified in all tests. For the case of Figure 4.2, it can be observed that the flow stress in all cases remains relatively constant for strains greater than 2.8%. We therefore focus on strain levels of 3% when comparing strength of micropillars, and conclude from Figure 4.4 that the numerical simulations quantitatively capture the flow stress, the highest deviation being the case of the 1 μm-diameter pillar.

The dislocation substructures found in a post-mortem specimen using transmission electron microscopy [21] supports the stage I easy-glide assumption for the strain range undergone by the specimens. Hardening rates from numerical simulations are in good agreement with experiments for sample diameters greater than 10 μm, in which both the magnitude and frequency of strain bursts are markedly reduced. As expected, numerical simulations do not introduce strain bursts in the mechanical response, since all the fields in the crystal plasticity model are continuous and smooth in time. The rate of hardening predicted by the model for sample diameters below 5 μm is apparently much higher than the rate found in experiments. However, these results should be interpreted in light of the recent studies by Shade et al. [83], where the effect of lateral constraints on the plastic response of micropillars is investigated. In particular, they show that low-friction top platen experiments, akin to roller top boundary conditions, result in almost no strain-hardening and large strain bursts, both of which are clearly observed in the 1, 2.5 and 5 μm sample-diameter experimental curves. By contrast, high-friction top platen resembling fully-restrained boundary conditions exhibit positive and increasing strain-hardening rates, with smaller and less frequent strain bursts. Since all simulations considered fully-restrained top boundary conditions, the observations of Shade and co-workers reconcile the numerical and experimental curves for sample diameters $\leq 5\mu$m.

The constrained-top experiments of Shade and co-workers show a barreled shape

of the compressed micropillar, together with a much more uniform distribution of slip traces along the height of the specimen than the unconstrained experiments, see Figure 4.5. This is also predicted by the simulations, and shown in Figure 4.6. The ability of the model to reproduce these features found in experiments is noteworthy.

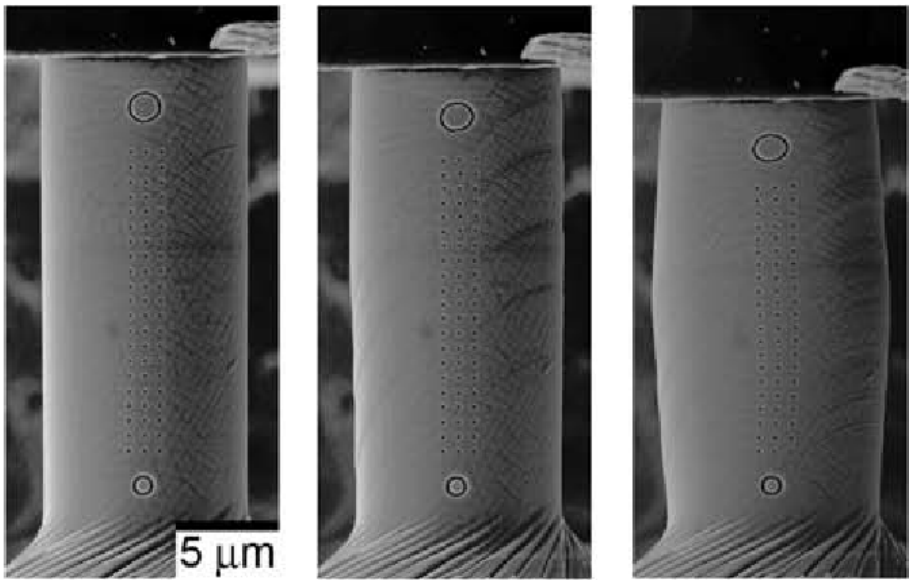

Figure 4.5: Ni superalloy micropillar - constrained experiment for axial strain 1%, 3% and 12%, from left to right.

The relation in experimental data between the resolved shear strength of micropillars and the sample diameter has been explained by several authors using a power-law expression of the form

$$\frac{\tau}{\mu} = A \left(\frac{d}{b}\right)^{M} \tag{4.1}$$

where A and M are constants found by fitting expression 4.1 to the data using least-squares regression. Dou and Derby [22] gathered data for Au, Ni, Cu and Al micropillars available from the literature, and obtained $A = 0.71$ and $M = -0.66$.

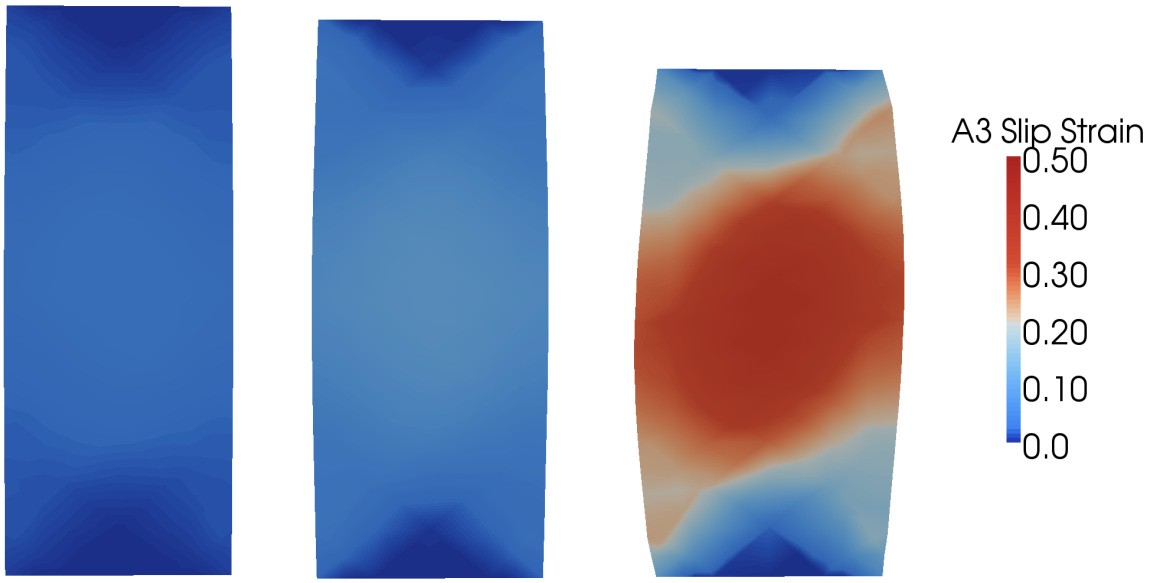

Figure 4.6: Ni micropillar simulation - A3 slip strain on deformed configuration for axial strain 1%, 3% and 12%, from left to right.

However, it should be noted that in their analysis, they included very different micropillar shapes, including circular and square cross sections, and crystal orientations, from the highly symmetrical [001] orientation where theoretically eight slip systems are active, to single-slip tests with the loading axis oriented in the [269] direction of the crystal. Dimiduk et al. [21] considered only the case of Ni micropillars and [269] loading direction, and performed a fit to the engineering stress in terms of the pillar diameter, which, after a simple conversion and normalization, yields constants $A = 0.35$ and $M = -0.64$ for diameters below 30 μm. We have also performed a fit of 4.1 to the flow stresses at 3% strain found in our numerical simulations, and obtained $A = 0.29$ and $M = -0.58$, which is in good agreement with previous values purely based on experimental results. Table 4.2 collects these values, and Figure 4.7 summarizes the analysis, showing the experimental values of Dimiduk et al., together

with the values obtained through numerical simulations and the corresponding fit.

Reference	A	M
Dou and Derby [22]	0.71	-0.66
Dimiduk et al.[21]	0.35	-0.64
This work	0.29	-0.58

Table 4.2: Power-law fit constants.

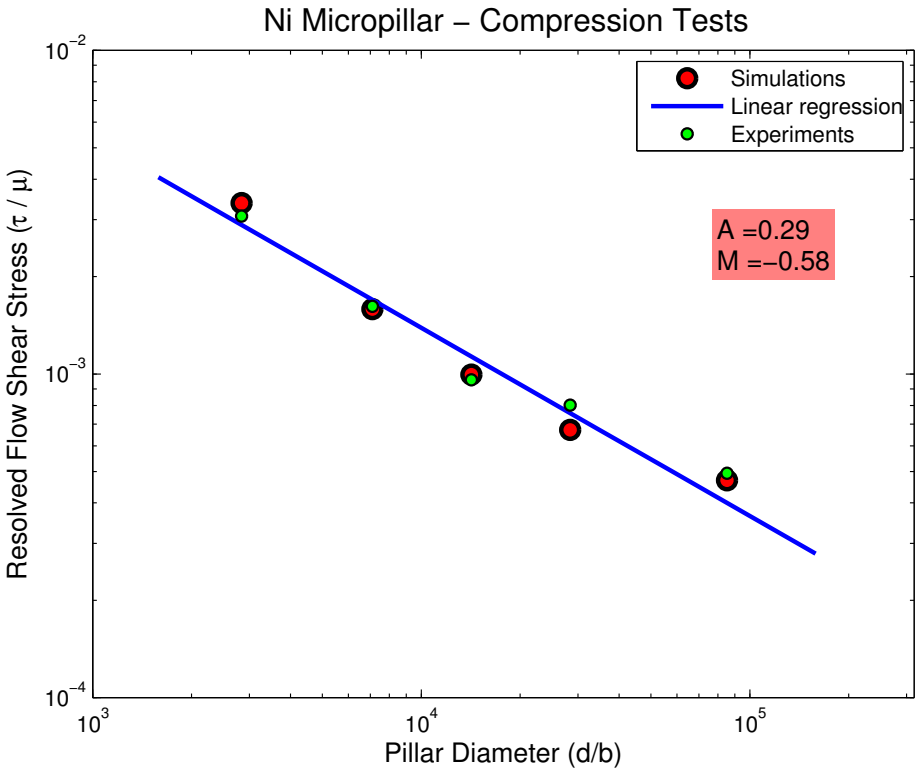

Figure 4.7: Micropillar strength - simulations and experiments.

The initial and post-mortem dislocation density of [269]-oriented Ni specimens has been measured by Norfleet and co-workers [68] for sample diameters ranging from 1 to 20 μm. On average, they found that the dislocation density in tested samples is greater than their estimated initial density, with a trend that the final density increases with

decreasing micropillar diameter. From our simulations, the GND density has been calculated using the expression 2.88, and average values of the GND density for the most active system (A3) have been obtained for $(\bar{1}11)$ planes located in the shear-band region. A comparison between the simulated and experimental final densities is shown in Figure 4.8. Although simulations qualitatively predict the trend that smaller pillars have greater final dislocation density, the orders of magnitude of experiments and simulations do not agree. However, we note that a direct comparison of these results is inconsequent, since the GND density represents only a fraction of the total dislocation density, to be complemented by the SSD density, whose evolution is not considered by the present model.

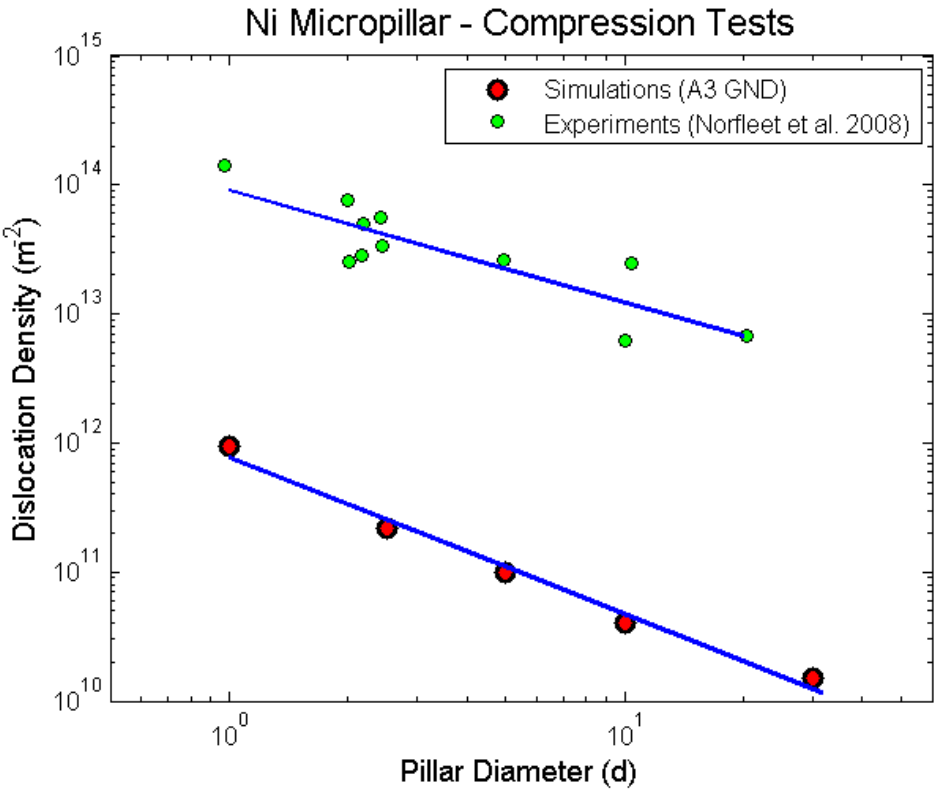

Figure 4.8: Dislocation Density - experiments and simulations.

Chapter 5

Conclusions

5.1 Summary

We have developed a novel physics-based multiscale model for the mechanical response of micromaterials. A continuum crystal plasticity formulation that takes into account the dislocation evolution in a continuous sense has been developed within a thermodynamic framework. The presented formulation considers the dislocation self-energy and the step formation energy, thus introducing a length scale that is otherwise not present in traditional crystal plasticity models.

Using the proposed model, we have performed numerical simulations of compression tests in nickel micropillars for different diameters, which quantitatively reproduce the size effect found in experiments. The predictive capabilities of the model developed in this work are noteworthy, especially considering that there is only one parameter to calibrate, the step energy, and that the calibration was done by considering only one experimental case.

Phenomenological strain-gradient plasticity methods based on the concept of geometrically necessary dislocations have been successful in explaining size effects in problems where the gradients of the strain field are relevant. However, dramatic size effects have been found in absence of significant gradients in the strain, and for such conditions strain-gradients theories fail to be predictive, highlighting the necessity of incorporating additional mechanisms. Surface effects can markedly influence the behavior of materials as the size of the samples is reduced, as demonstrated by the proposed model. In particular, the surfaces of samples fabricated using the FIB technique are known to have severe damage, which has been observed and measured in terms of Ga^{+} penetration and atomic percentage. However, to the best of our knowledge, the mechanical properties of FIB damaged surfaces have not been assessed, and thus surface damage has been largely neglected in the mechanical modeling of micropillar. The proposed mechanical model could provide with an estimate for the step energy in damaged materials based on the fit done to experiments, which remains to be corroborated experimentally.

Due to their complexity, multiscale simulations are computationally very demanding. Therefore, the scalability of a numerical algorithm is critical to the success of the method. In this work, we have demonstrated the high scalability of the method for small-to-moderate meshes that do not require domain decomposition. Moreover, we have provided a closed-form solution to the discretized vector-potential problem, which is also highly scalable due to the little communication requirements.

5.2 Future work

Many aspects of the theory presented here can be the subject of further study. An interesting avenue to pursue is the connection between the line tension model resulting from the assumption of continuously distributed dislocations and dislocation dynamics. In particular, we have assumed that line tension is isotropic and constant throughout the crystal. For example, the line tension values could be obtained from dislocation dynamic simulations that are representative of the dislocation substructure typically found in micromaterials. Theoretical results supporting this connection have been recently developed by Garroni and Müller [33].

We have considered a simple phenomenological expression for the local plastic energy that proves sufficient for the stage I easy-glide regime observed in micropillar compression tests. In particular, dislocation interaction leading to latent hardening is not predominant in this setting, due to the orientation of the pillar lattice, which favors the activation of only one slip system. A physics-based forest-dislocation hardening model that accounts for dislocation interaction and has been successful in predicting stage I and II in single crystals was developed by Cuitino and Ortiz [17]. In their formulation, the dislocation density results from the solution of a simple evolution equation, which is in one-to-one correspondence with the slip strain. Since the present model provides the GND density as a result, we could directly provide

the dislocation density to the forest-dislocation hardening model of Cuitino and Ortiz.

The numerical simulations presented here are restricted to nickel single-crystal micropillars. A natural extension using the same framework is the study of other materials that have also been experimentally investigated, like Au, Cu and Al. Likewise, the present model could be also employed in the simulation of much smaller samples with nanometer dimensions, where surface effects are expected to take an even stronger role in the mechanical response.

Appendix A

Total variation

Definition 1 (Total Variation)**.** *Given a function $f \in L^1(\Omega)$, the total variation is defined as*

$$V(f,\Omega) := \sup_{\substack{\phi \in C_c^1(\Omega,\mathbb{R}^n) \\ ||\phi||_{L^\infty(\Omega)} \leq 1}} \int_\Omega f \ \mathrm{div}\, \phi \ \mathrm{d}V$$

Remark 1. *If $f \in C^1(\Omega)$ it can be shown that*

$$V(f,\Omega) = \int_\Omega |\nabla f| \, \mathrm{d}V$$

Moreover, it can also be shown that

$$\begin{aligned} V_{P^\alpha}(f,\Omega) := \int_\Omega |\nabla_{P^\alpha} f| \, \mathrm{d}V &= \sup_{\substack{\phi \in C_c^1(\Omega,\mathbb{R}^n) \\ ||\phi||_{L^\infty(\Omega)} \leq 1}} \int_\Omega f \, \mathrm{div}(\mathcal{P}^\alpha \phi) \, \mathrm{d}V \\ &= \sup_{\substack{\phi \in C_c^1(\Omega,\mathbb{R}^n) \\ ||\phi||_{L^\infty(\Omega)} \leq 1}} \int_\Omega f \mathcal{P}^\alpha : \nabla \phi \, \mathrm{d}V \end{aligned} \tag{A.1}$$

where $\mathcal{P}^\alpha$ is the orthogonal-projection operator defined in B.5, and $:$ denotes the tensor

full-contraction operation.

Appendix B

In-plane gradient derivation

Let $\boldsymbol{M} \in \mathbb{R}^{n\times n}$. The Frobenius norm for square real matrices is defined as

$$\|\boldsymbol{M}\|_2 = \sqrt{M_{ij}M_{ij}} = \sqrt{\text{Trace}(\boldsymbol{M}^T\boldsymbol{M})} \tag{B.1}$$

Now, consider the case $\boldsymbol{M} = \boldsymbol{s}^\alpha \otimes (\nabla\gamma^\alpha \times \boldsymbol{m}^\alpha)$. Then we have

$$\|\boldsymbol{M}\|_2 = \sqrt{(\boldsymbol{s}^\alpha \cdot \boldsymbol{s}^\alpha)\,(\nabla\gamma^\alpha \times \boldsymbol{m}^\alpha \cdot \nabla\gamma^\alpha \times \boldsymbol{m}^\alpha)} \tag{B.2}$$

however, $(\boldsymbol{s}^\alpha \cdot \boldsymbol{s}^\alpha) = 1$ by definition. Continuing in indicial notation we have

$$\begin{aligned}
\|\boldsymbol{M}\|_2 &= \sqrt{\epsilon_{ipq}\gamma^\alpha_{,p}m_q\epsilon_{irs}\gamma^\alpha_{,r}m_s} \\
&= \sqrt{(\delta_{pr}\delta_{qs} - \delta_{ps}\delta_{rq})\gamma^\alpha_{,p}m_q\gamma^\alpha_{,r}m_s} \\
&= \sqrt{\gamma^\alpha_{,p}\gamma^\alpha_{,p} - \gamma^\alpha_{,s}m_s\gamma^\alpha_{,q}m_q} \\
&= \sqrt{\|\nabla\gamma^\alpha\|^2 - \|\frac{\partial\gamma^\alpha}{\partial\boldsymbol{m}^\alpha}\|^2}
\end{aligned} \tag{B.3}$$

where we have used the tensorial identity $\epsilon_{ipq}\epsilon_{irs} = \delta_{pr}\delta_{qs} - \delta_{ps}\delta_{rq}$ and the fact that $\boldsymbol{m}^\alpha \cdot \boldsymbol{m}^\alpha = 1$. The expression B.3 is clearly the Euclidean norm of the projection of the vector $\nabla\gamma^\alpha$ onto the plane defined by the plane-normal $\boldsymbol{m}^\alpha$. Equivalently, let the *in-plane gradient* be

$$\nabla_{P^\alpha}\gamma^\alpha = \mathcal{P}^\alpha \nabla\gamma^\alpha \tag{B.4}$$

where

$$\mathcal{P}^\alpha = \boldsymbol{I} - \boldsymbol{m}^\alpha \otimes \boldsymbol{m}^\alpha \tag{B.5}$$

is the *orthogonal-projection operator*. Then it is readily verified that

$$\|\boldsymbol{M}\|_2 = \|\nabla_{P^\alpha}\gamma^\alpha\|_2 \tag{B.6}$$

Appendix C

Submersion mapping and its tangents

Let $GL_+(3) = \left\{\boldsymbol{X} \in \mathbb{R}^{3\times3} | \det \boldsymbol{X} > 0\right\}$ be the general linear group, and $SL(3) = \left\{\boldsymbol{Y} \in \mathbb{R}^{3\times3} | \det \boldsymbol{Y} = 1\right\}$ be the special linear group, such that $SL(3) \subset GL_+(3)$. Consider the submersion mapping $g : GL_+(3) \to SL(3)$ given by

$$g(\boldsymbol{X}) = \frac{\boldsymbol{X}}{\det^{\frac{1}{3}}(\boldsymbol{X})} \tag{C.1}$$

or in component notation

$$g_{ij}(\boldsymbol{X}) = \frac{X_{ij}}{\det^{\frac{1}{3}}(\boldsymbol{X})} \tag{C.2}$$

Moreover, recall the identities

$$\frac{\partial \det(\boldsymbol{X})}{\partial X_{ij}} = \mathrm{adj}(\boldsymbol{X})_{ij} = \det(\boldsymbol{X}) X^{-1}_{ji} \tag{C.3}$$

$$\frac{\partial X^{-1}_{ji}}{\partial X_{kl}} = -X^{-1}_{jk} X^{-1}_{li} \tag{C.4}$$

Then, it can be shown that the first tangent of the submersion mapping is

$$\frac{\partial g_{ij}(\boldsymbol{X})}{\partial X_{kl}} = \det{}^{-\frac{1}{3}}(\boldsymbol{X}) \left\{ \delta_{ik}\delta_{jl} - \frac{1}{3} X^{-1}_{lk} X_{ij} \right\} \tag{C.5}$$

$$= \det{}^{-\frac{1}{3}}(\boldsymbol{X})\, \delta_{ik}\delta_{jl} - \frac{1}{3} X^{-1}_{lk} g_{ij}(\boldsymbol{X}) \tag{C.6}$$

and the second tangent is given by

$$\frac{\partial^2 g_{ij}(\boldsymbol{X})}{\partial X_{pq} \partial X_{kl}} = -\frac{1}{3} \left\{ \det{}^{-\frac{1}{3}}(\boldsymbol{X}) X^{-1}_{qp} \delta_{ik}\delta_{jl} - X^{-1}_{lp} X^{-1}_{qk}\, g_{ij}(\boldsymbol{X}) + X^{-1}_{lk} \frac{\partial g_{ij}(\boldsymbol{X})}{\partial X_{pq}} \right\} \tag{C.7}$$

$$= -\frac{1}{3} \det{}^{-\frac{1}{3}}(\boldsymbol{X}) \left\{ X^{-1}_{qp}\delta_{ik}\delta_{jl} + X^{-1}_{lk}\delta_{ip}\delta_{jq} - \left(X^{-1}_{lp} X^{-1}_{qk} + \frac{1}{3} X^{-1}_{lk} X^{-1}_{qp} \right) X_{ij} \right\} \tag{C.8}$$

Bibliography

[1] A. Acharya and J. L. Bassani, *Lattice incompatibility and gradient theory of crystal plasticity*, Journal of the Mechanics and Physics of Solids **48** (2000), 1565–1595.

[2] R.J. Amodeo and N.M. Ghoniem, *Dislocation dynamics. 1. A proposed methodology for deformation micromechanics*, Physical Review B **41** (1990), no. 10, Part B, 6958–6967.

[3] ———, *Dislocation dynamics. 2. Applications to the formation of persistent slip bands, planar arrays and dislocation cells*, Physical Review B **41** (1990), no. 10, Part B, 6968–6976.

[4] B. Arnold, D. Lohse, Bauer H., T. Gemming, K. Wetzig, and K. Binder, *Surface damages on FIB prepared TEM-specimens: possibilities of avoidance and removal*, Microscopy and Microanalysis **9** (2003), 140–141.

[5] A. Arsenlis and D.M. Parks, *Crystallographic aspects of geometrically-necessary and statistically-stored dislocation density*, Acta Materialia **47** (1999), no. 5, 1597–1611.

[6] A Arsenlis and D.M. Parks, *Modeling the evolution of crystallographic dislocation*

density in crystal plasticity, Journal of the Mechanics and Physics of Solids **50** (2002), no. 9, 1979–2009.

[7] R.J. Asaro and V.A. Lubarda, *Mechanics of Solids and Materials*, Cambridge University Press, 2006.

[8] R.J. Asaro and J.R. Rice, *Strain localization in ductile single-crystals*, Journal of the Mechanics and Physics of Solids **25** (1977), no. 5, 309–338.

[9] M.F. Ashby, *Deformation of plastically non-homogeneous materials*, Philosophical Magazine **21** (1970), no. 170, 399–424.

[10] V.L. Berdichevsky, *Continuum theory of dislocations revisited*, Continuum Mechanics and Thermodynamics **18** (2006), no. 3-4, 195–222.

[11] ———, *Variational Principles of Continuum Mechanics, I. Fundamentals*, Springer-Verlag Berlin, 2009.

[12] B.A. Bilby, R. Bullough, and E. Smith, *Continuous distributions of dislocations - A new application of the methods of non-Riemannian geometry*, Proceedings of the Royal Society of London Series A-Mathematical and Physical Sciences **231** (1955), no. 1185, 263–273.

[13] S. Boyd and L. Vandenbergue, *Convex Optimization*, Cambridge University Press, 2004.

[14] S.S. Brenner, *Tensile strength of whiskers*, Journal of Applied Physics **27** (1956), no. 12, 1484–1491.

[15] M. Crouzeix and P.A. Raviart, *Conforming and nonconforming finite-element methods for solving stationary stokes equations*, Revue Francaise D' Automatique Informatique Recherche Operationnelle **7** (1973), no. DEC, 33–75.

[16] A.M. Cuitino and M. Ortiz, *A material-independent method for extending stress update algorithms from small-strain plasticity to finite plasticity with multiplicative kinematics*, Engineering Computations **9** (1992), 437–451.

[17] ———, *Computational modeling of single-crystals*, Modelling and Simulation in Materials Science and Engineering **1** (1993), no. 3, 225–263.

[18] ———, *Constitutive modeling of Ll2 intermetallic crystals*, Materials Science and Engineering A-Structural Materials Properties Microstructure and Processing **170** (1993), no. 1-2, 111–123.

[19] M. Dao, L. Lu, R. J. Asaro, J.T.M. De Hosson, and E. Ma, *Toward a quantitative understanding of mechanical behavior of nanocrystalline metals*, Acta Materialia **55** (2007), no. 12, 4041–4065.

[20] B. Devincre and M. Condat, *Model validation of a 3d simulation of dislocation dynamics - Discretization and line tension effects*, Acta Metallurgica et Materialia **40** (1992), no. 10, 2629–2637.

[21] D.M. Dimiduk, M.D. Uchic, and T.A. Parthasarathy, *Size-affected single-slip behavior of pure nickel microcrystals*, Acta Materialia **53** (2005), no. 15, 4065–4077.

[22] R. Dou and B. Derby, *A universal scaling law for the strength of metal micropillars and nanowires*, Scripta Materialia **61** (2009), no. 5, 524–527.

[23] A. Ern and J.L. Guermond, *Theory and Practice of Finite Elements*, Springer-Verlag, 2004.

[24] A.L. Eterovic and K.J. Bathe, *A hyperelastic-based large strain elastoplastic constitutive formulation with combined isotropic-kinematic hardening using the logarithmic stress and strain measures*, International Journal for Numerical Methods in Engineering **30** (1990), no. 6, 1099–1114.

[25] J.A. Ewing and W. Rosenhain, *The crystalline structure of metals*, Proceedings of the Royal Society of London **193** (1900), 353–375.

[26] C.A. Felippa, K.C. Park, and C. Farhat, *Partitioned analysis of coupled mechanical systems*, Computer Methods in Applied Mechanics and Engineering **190** (2001), no. 24-25, 3247–3270.

[27] N.A. Fleck and J.W. Hutchinson, *A phenomenological theory for strain gradient effects in plasticity*, Journal of the Mechanics and Physics of Solids **41** (1993), no. 12, 1825–1857.

[28] ———, *Strain gradient plasticity*, Advances in Applied Mechanics **33** (1997), 295–361.

[29] ———, *A reformulation of strain gradient plasticity*, Journal of the Mechanics and Physics of Solids **49** (2001), no. 10, 2245–2271.

[30] N.A. Fleck, G.M. Muller, M.F. Ashby, and J.W. Hutchinson, *Strain gradient plasticity: theory and experiment*, Acta Metallurgia Materalia **42** (1994), no. 2, 475–487.

[31] P. Franciosi and A. Zaoui, *Multislip in FCC Crystals : A theoretical approach compared with experimental data*, Acta Metallurgica **30** (1982), no. 8, 1627–1637.

[32] J. Frenkel, *Zur Theorie der Elastizittsgrenze und der Festigkeit kristallinischer Krper*, Zeitschrift fr Physik A Hadrons and Nuclei **37** (1926), 572–609.

[33] A. Garroni and S. Muller, *A variational model for dislocations in the line tension limit*, Archive for Rational Mechanics and Analysis **181** (2006), no. 3, 535–578.

[34] J.J. Gilman, *Micromechanics of flow in solids*, McGraw-Hill, 1969.

[35] J.R. Greer and W.D. Nix, *Nanoscale gold pillars strengthened through dislocation starvation*, Physical Review B **73** (2006), no. 24.

[36] J.R. Greer, W.C. Oliver, and W.D. Nix, *Size dependence of mechanical properties of gold at the micron scale in the absence of strain gradients*, Acta Materialia **53** (2005), no. 6, 1821–1830.

[37] M.E. Gurtin, *On the plasticity of single crystals: free energy, microforces, plastic-strain gradients*, Journal of the Mechanics and Physics of Solids **48** (2000), no. 5, 989–1036.

[38] ———, *A gradient theory of single-crystal viscoplasticity that accounts for geo-*

metrically necessary dislocations, Journal of the Mechanics and Physics of Solids **50** (2002), no. 1, 5–32.

[39] E.O. Hall, *The deformation and ageing of mild steel: III Discussion of Results*, Proceedings of the Physical Society. Section B **64** (1951), no. 9, 747.

[40] P. Hauret, E. Kuhl, and M. Ortiz, *Diamond elements: A finite element/discrete-mechanics approximation scheme with guaranteed optimal convergence in incompressible elasticity*, International Journal for Numerical Methods in Engineering **72** (2007), no. 3, 253–294.

[41] K.S. Havner, *Mechanics of crystalline solids*, Journal of the Mechanics and Physics of Solids **21** (1973), no. 6, 383–394.

[42] R. Hill, *Generalized constitutive relations for incremental deformation of metal crystals by multislip*, Journal of the Mechanics and Physics of Solids **14** (1966), no. 2, 95–102.

[43] R. Hill and J.R. Rice, *Constitutive analysis of elastic-plastic crystals at arbitrary strain*, Journal of the Mechanics and Physics of Solids **20** (1972), no. 6, 401–413.

[44] J.P. Hirth and J. Lothe, *Theory of Dislocations*, John Wiley & Sons, 1982.

[45] T.J.R. Hughes, *Generalization of selective integration procedures to anisotropic and non-linear media*, International Journal for Numerical Methods in Engineering **15** (1980), no. 9, 1413–1418.

[46] ———, *The Finite Element Method - Linear Static and Dynamic Finite Element Analysis*, Dover Publications, 2000.

[47] D. Kiener, C. Motz, M. Rester, M. Jenko, and G. Dehm, *FIB damage of Cu and possible consequences for miniaturized mechanical tests*, Materials Science and Engineering A-Structural Materials Properties Microstructure and Processing **459** (2007), no. 1-2, 262–272.

[48] D. Kiener, C. Motz, T. Schoeberl, M. Jenko, and G. Dehm, *Determination of mechanical properties of copper at the micron scale*, Advanced Engineering Materials **8** (2006), no. 11, 1119–1125.

[49] U.F. Kocks, *Polyslip in single crystals*, Acta Metallurgica **8** (1960), no. 6, 345–352.

[50] J. Kratochvl, *On a finite strain theory of elastic-inelastic materials*, Acta Mechanica **16** (1973), 127–142.

[51] E. Kröner, *Allgemeine Kontinuumstheorie der Versetzungen und Eigenspannungen*, Archive for Rational Mechanics and Analysis **4** (1959), 273–334.

[52] K.C. Le and P. Sembiring, *Analytical solution of plane constrained shear problem for single crystals within continuum dislocation theory*, Archive of Applied Mechanics **78** (2008), no. 8, 587–597.

[53] ———, *Plane constrained shear of single crystal strip with two active slip systems*, Journal of the Mechanics and Physics of Solids **56** (2008), no. 8, 2541–2554.

[54] E.H. Lee, *Elastic-plastic deformation at finite strains*, Journal of Applied Mechanics **36** (1969), no. 1, 1–&.

[55] J Lepinoux and L.P. Kubin, *The dynamic organization of dislocation-structures - A simulation*, Scripta Metallurgica **21** (1987), no. 6, 833–838.

[56] J. Lubliner, *On the thermodynamic foundations of non-linear solid mechanics*, International Journal of Non-Linear Mechanics **7** (1972), no. 3, 237–254.

[57] ———, *On the structure of rate equations of materials with internal variables*, Acta Mechanica **17** (1973), no. 1-2, 109–119.

[58] F. Machalett, K. Edinger, J. Melngailis, M. Diegel, K. Steenbeck, and E. Steinbeiss, *Direct patterning of gold oxide thin films by focused ion-beam irradiation*, Applied Physics A-Materials Science & Processing **71** (2000), no. 3, 331–335.

[59] J.E. Marsden and T.J.R. Hughes, *Mathematical foundations of elasticity* , Dover Publications, 1994.

[60] J.E. Marsden and T.S. Ratiu, *Introduction to mechanics and symmetry*, Springer-Verlag New York, 1999.

[61] C. Miehe, *Exponential map algorithm for stress updates in anisotropic multiplicative elastoplasticity for single crystals*, International Journal for Numerical Methods in Engineering **39** (1996), no. 19, 3367–3390.

[62] H.-B. Mühlhaus and E.C. Aifantis, *A variational principle for gradient plasticity*, International Journal of Solids and Structures **28** (1991), no. 7, 845–857.

[63] J.C. Nagtegaal, D.M. Parks, and J.R. Rice, *On numerically accurate finite element solutions in the fully plastic range*, Computer Methods in Applied Mechanics and Engineering **4** (1974), no. 2, 153–177.

[64] A Needleman, *Computational mechanics at the mesoscale*, Acta Materialia **48** (2000), no. 1, 105–124.

[65] A. Needleman and E. Van der Giessen, *Discrete dislocation and continuum descriptions of plastic flow*, Materials Science and Engineering A-Structural Materials Properties Microstructure and Processing **309** (2001), no. Sp. Iss. SI, 1–13.

[66] K.S. Ng and A.H.W. Ngan, *Stochastic nature of plasticity of aluminum micropillars*, Acta Materialia **56** (2008), no. 8, 1712–1720.

[67] W.D. Nix and H.J. Gao, *Indentation size effects in crystalline materials: A law for strain gradient plasticity*, Journal of the Mechanics and Physics of Solids **46** (1998), no. 3, 411–425.

[68] D.M. Norfleet, D.M. Dimiduk, S.J. Polasik, M.D. Uchic, and M.J. Mills, *Dislocation structures and their relationship to strength in deformed nickel microcrystals*, Acta Materialia **56** (2008), no. 13, 2988–3001.

[69] J.F. Nye, *Some geometrical relations in dislocated crystals*, Acta Metallurgica **1** (1953), no. 2, 153 – 162.

[70] E. Orowan, *Zur kristallplastizität III. über den mechsnismus des gleitvorganges*, Zeitschrift für Physik **89** (1934), 634–659.

[71] M. Ortiz, *Computational Mechanics - Course Notes*, 2009.

[72] ———, *Continuum Mechanics - Course Notes*, 2009.

[73] M. Ortiz, R.A. Radovitzky, and E.A. Repetto, *The computation of the exponential and logarithmic mappings and their first and second linearizations*, International Journal for Numerical Methods in Engineering **52** (2001), no. 12, 1431–1441.

[74] M. Ortiz and E.A. Repetto, *Nonconvex energy minimization and dislocation structures in ductile single crystals*, Journal of the Mechanics and Physics of Solids **47** (1999), no. 2, 397–462.

[75] M. Ortiz and L. Stainier, *The variational formulation of viscoplastic constitutive updates*, Computer Methods in Applied Mechanics and Engineering **171** (1999), no. 3-4, 419–444.

[76] D. Peirce, R.J. Asaro, and A. Needleman, *Material rate dependence and localized deformation in crystalline solids*, Acta Metallurgica **31** (1983), no. 12, 1951–1976.

[77] N. J. Petch, *The cleavage strength of polycrystals*, Journal of the Iron and Steel Institute **174** (1953), no. 25, 8.

[78] M. Polanyi, *Gitterstörung die einen kristall plastisch machen könnte*, Zeitschrift für Physik (1934), no. 89, 660–664.

[79] R. Radovitzky and M. Ortiz, *Error estimation and adaptive meshing in strongly nonlinear dynamic problems*, Computer Methods in Applied Mechanics and Engineering **172** (1999), no. 1-4, 203–240.

[80] J.R. Rice, *Inelastic constitutive relations for solids - An internal-variable theory and its application to metal plasticity*, Journal of the Mechanics and Physics of Solids **19** (1971), no. 6, 433–&.

[81] P. Rosakis, A.J. Rosakis, G. Ravichandran, and J. Hodowany, *A thermodynamic internal variable model for the partition of plastic work into heat and stored energy in metals*, Journal of the Mechanics and Physics of Solids **48** (2000), no. 3, 581–607.

[82] B. Schmidt, F. Fraternali, and M. Ortiz, *Eigenfracture: An eigendeformation approach to variational fracture*, Multiscale Modeling & Simulation **7** (2009), no. 3, 1237–1266.

[83] P.A. Shade, R. Wheeler, Y.S. Choi, M.D. Uchic, D.M. Dimiduk, and H.L. Fraser, *A combined experimental and simulation study to examine lateral constraint effects on microcompression of single-slip oriented single crystals*, Acta Materialia **57** (2009), no. 15, 4580–4587.

[84] G. Simmonds and H. Wang, *Single Crystal Elastic Constants and Calculated Aggregate Properties*, MIT Press, Cambridge, MA, 1971.

[85] J.C. Simo and T.J.R. Hughes, *Computational Inelasticity*, Springer-Verlag, New York, 1998.

[86] N.A. Stelmashenko, M.G. Walls, L.M. Brown, and Y.V. Milman, *Microindentations on W and MO oriented single-crystals - An STM study*, Acta Metallurgica et Materialia **41** (1993), no. 10, 2855–2865.

[87] J.S. Stolken and A.G. Evans, *A microbend test method for measuring the plasticity length scale*, Acta Materialia **46** (1998), no. 14, 5109–5115.

[88] G.I. Taylor, *The mechanism of plastic defomration of crystals part I.- Theoretical*, Proceedings of the Royal Society of London (1934), no. A145, 362–387.

[89] ———, *Plastic strain in metals*, Journal of the Institute of Metals **62** (1938), no. 1, 307–324.

[90] M.D. Uchic, D.M. Dimiduk, J.N. Florando, and W.D. Nix, *Sample dimensions influence strength and crystal plasticity*, Science **305** (2004), no. 5686, 986–989.

[91] F.L. Vogel, W.G. Pfann, H.E. Corey, and E.E. Thomas, *Observations of dislocations in lineage boundaries in germanium*, Physical Review **90** (1953), no. 3, 489–490.

[92] G. Weber and L. Anand, *Finite deformation constitutive-equations and a time integration procedure for isotropic, hyperelastic viscoplastic solids*, Computer Methods in Applied Mechanics and Engineering **79** (1990), no. 2, 173–202.

[93] Q. Yang, L. Stainier, and M. Ortiz, *A variational formulation of the coupled thermo-mechanical boundary-value problem for general dissipative solids*, Journal of the Mechanics and Physics of Solids **54** (2006), no. 2, 401–424.

[94] H. M. Zbib and E. C. Aifantis, *A gradient-dependent flow theory of plasticity: application to metal and soil instabilities*, Applied Mechanics Reviews **42** (1989), no. 11S, S295–S304.